

September 2019

# Molecular Weight and Thermal Properties of Fiber Reinforced Polyamide-Based Composites Throughout the Direct Long-Fiber Reinforced Thermoplastic Process

Mingyu Yang

*The University of Western Ontario*

Supervisor

Kuboki, Takashi

*The University of Western Ontario*

Co-Supervisor

Wood, Jeffrey T

*The University of Western Ontario*

Graduate Program in Mechanical and Materials Engineering

A thesis submitted in partial fulfillment of the requirements for the degree in Master of Engineering Science

© Mingyu Yang 2019

Follow this and additional works at: <https://ir.lib.uwo.ca/etd>



Part of the [Materials Science and Engineering Commons](#)

---

## Recommended Citation

Yang, Mingyu, "Molecular Weight and Thermal Properties of Fiber Reinforced Polyamide-Based Composites Throughout the Direct Long-Fiber Reinforced Thermoplastic Process" (2019). *Electronic Thesis and Dissertation Repository*. 6431.

<https://ir.lib.uwo.ca/etd/6431>

## Abstract

The D-LFT process is an efficient and cost-effective process and includes two twin-screw extruders, a conveyor, and a compression molding machine. It is imperative to understand how the process sequence affects molecular weight and thermal properties of composite materials during the D-LFT process. The main objective of this study was to characterize variation in molecular weight and thermal properties of two types of polyamide (PA)-based composite materials (glass fiber reinforced PA6 composites and carbon fiber reinforced PA66 composites) through the D-LFT process. Samples were taken from different locations along the D-LFT process and characterized using triple detection gel permeation chromatography (GPC), thermogravimetric analysis (TGA), differential scanning calorimetry (DSC), and fourier-transform infrared spectroscopy (FTIR). It was found that molecular weight of both PA-based composites increased after the second extruder by branching of PA molecules. Therefore, process conditions after the second extruder need to be carefully adjusted to design PA-based D-LFT products.

### **Keywords**

Polyamides, Fibers, Composites, Processing, D-LFT, Molecular Weight, Thermal Properties

## Summary for Lay Audience

Driven by economic, legislative and market considerations, light weight design has become one of the core design principles in transportation industry all around the globe in the last few decades. Composite materials have emerged as a front running solution to the light-weighting challenge, as they are lighter than other competitor materials such as steel and aluminum and can be tailor-made to a specific application. The direct long-fiber reinforced thermoplastic (D-LFT) process is an efficient and cost-effective process to manufacture long-fiber reinforced thermoplastics. Polyamide (PA)-based composite materials manufactured through the D-LFT process are good candidates to be used for products where mechanical and thermal loadings are exerted. In this study, thermal properties of two types of PA-based composite materials were investigated at different locations along the D-LFT process, and the process location that is important to design PA-based D-LFT products was identified.

## Co-Authorship Statement

1.

Title: Effects of Extruder Screw Configurations on Thermal Properties of Glass Fiber Reinforced Polyamide 6 Composites throughout the Direct Long-Fiber Reinforced Thermoplastics Process (Chapter 2)

Authors: Mingyu Yang<sup>1</sup>, Takashi Kuboki<sup>1</sup>, Jeffrey Wood<sup>1</sup>, Vanja Ugresic<sup>2</sup>

1. Department of Mechanical and Materials Engineering, University of Western Ontario, London, Ontario, Canada, N6A 5B9
2. Fraunhofer Project Centre for Composites Research, University of Western Ontario, London, Ontario, Canada, N6M 0E1

Mingyu Yang collected, analyzed, and interpreted the data under the constructive suggestions of Dr. Takashi Kuboki. Mingyu Yang drafted the manuscript under the guidance of Dr. Takashi Kuboki, and the manuscript was revised by Dr. Takashi Kuboki and Dr. Jeffrey Wood. Manufacturing of the composites was conducted by Vanja Ugresic. The manuscript was accepted by Polymer Composites.

2.

Title: Molecular Weight and Thermal Properties of Carbon Fiber Reinforced Polyamide 66 Composites throughout the Direct Long-Fiber Reinforced Thermoplastics Process (Chapter 3)

Authors: Mingyu Yang<sup>1</sup>, Takashi Kuboki<sup>1</sup>, Jeffrey Wood<sup>1</sup>, Vanja Ugresic<sup>2</sup>

1. Department of Mechanical and Materials Engineering, University of Western Ontario, London, Ontario, Canada, N6A 5B9

2. Fraunhofer Project Centre for Composites Research, University of Western Ontario,  
London, Ontario, Canada, N6M 0E1

Mingyu Yang collected, analyzed, and interpreted the data under the constructive suggestions of Dr. Takashi Kuboki. Mingyu Yang drafted the manuscript under the guidance of Dr. Takashi Kuboki, and the manuscript was revised by Dr. Takashi Kuboki and Dr. Jeffrey Wood. Manufacturing of the composites was conducted by Vanja Ugresic. The manuscript will be submitted for publication.

## Acknowledgments

I would first like to express my gratitude to my supervisors, Dr. Takashi Kuboki and Dr. Jeffrey Wood, for providing me this valuable opportunity to pursue this project as a part of my M.E.Sc. study program. Their guidance, patience and constructive feedback throughout my master study not only helped me with the subject matter, but also helped me acquire the correct research attitude.

I would further acknowledge the contributions of Dr. Ying Fan to my project, especially for lab training, which facilitated smooth conduction of tests. I am also grateful to Dr. Liying Jiang, Dr. Ovidiu-Remus Tutunea-Fatan, and Dr. Wenxing Zhou for being my examiners. I would also like to thank the academic, technical and administrative staff at Department of Mechanical and Materials Engineering at the University of Western Ontario for being ever so committed to being helpful to students like me. Credit for the successful completion of this project must also be given to Ms. Vanja Ugresic, along with the staff at Fraunhofer Project Center, who made the premises and facilities available and enabled the investigation of process parameters in D-LFT process on the thermal properties of composites.

I am also grateful for the financial support provided by Automotive Partnership Canada (APC), BASF Corporation, ElringKlinger Canada Inc., Dieffenbacher North America, General Motors of Canada Company (GM), and Johns Manville.

Finally, I would like to appreciate the support and backing of Aaditya Suratkar, my close friend and colleague, my family, and other well-wishers in the university.

## Table of Contents

Abstract.....	i
Summary for Lay Audience .....	ii
Co-Authorship Statement.....	iii
Acknowledgments .....	1
Table of Contents .....	2
List of Tables.....	6
List of Figures .....	7
Chapter 1 .....	10
1 Introduction .....	10
1.1. Composites .....	10
1.1.1. Reinforcement.....	12
1.1.2. Matrix .....	14
1.1.3. Reinforcement-matrix Interface .....	16
1.2. Background.....	17
1.2.1. Long-fiber Reinforced Thermoplastics .....	17
1.2.2. Processing Techniques .....	17
1.2.3. Candidate Materials for D-LFT Process.....	20
1.2.3.1. Fibers .....	20
1.2.3.1.1. Glass Fibers .....	20
1.2.3.1.2. Carbon Fibers .....	22
1.2.3.1. Matrix.....	24

1.2.3.1.1.	Polyamides .....	24
1.2.3.1.2.	Polyamide 6 and Polyamide 66 .....	25
1.2.3.1.3.	Possible Reactions Through D-LFT Process.....	26
1.2.3.1.3.1.	Thermal Reaction .....	27
1.2.3.1.3.1.1.	Chain Scission .....	27
1.2.3.1.3.1.2.	Branching .....	29
1.2.3.1.3.2.	Thermal Oxidation Reaction .....	30
1.2.3.1.3.2.1.	Chain Scission .....	30
1.2.3.1.3.2.2.	Branching .....	35
1.3.	Research Background.....	36
1.4.	Objectives .....	36
1.5.	Significance .....	37
	References .....	38
	Chapter 2.....	44
2	Effects of Extruder Screw Configurations on Thermal Properties of Glass Fiber-Reinforced Polyamide 6 Composites throughout the Direct Long-Fiber-Reinforced Thermoplastics Process .....	44
2.1.	Introduction .....	44
2.1	Experimental.....	47
2.1.1	Materials and fabrication of composites.....	47
2.1.2	Triple detection gel permeation chromatography (GPC) .....	48
2.1.3	Thermogravimetric analysis.....	50
2.1.4	Differential scanning calorimetry.....	51



2.2 Results and Discussion.....	53
2.2.1 Discoloration.....	53
2.2.2 Molecular weight and intrinsic viscosity.....	54
2.2.3 Thermal decomposition.....	57
2.2.4 Crystallization.....	59
2.2.4.1 Non-Isothermal Crystallization.....	59
2.2.4.2 Isothermal Crystallization.....	62
2.3 Conclusions.....	66
References.....	67
Chapter 3.....	73
3 Molecular Weight and Thermal Properties of Carbon Fiber Reinforced Polyamide 66 Composites throughout the Direct Long-Fiber Reinforced Thermoplastics Process.....	73
3.1 Introduction.....	73
3.2 Experimental.....	76
3.2.1 Materials and fabrication of composites.....	76
3.2.2 Triple detection gel permeation chromatography (GPC).....	77
3.2.3 Thermogravimetric analysis.....	78
3.2.4 Differential scanning calorimetry.....	79
3.2.5 Fourier-transform infrared spectroscopy.....	81
3.3 Results and Discussion.....	82
3.3.1 Discoloration.....	82
3.3.2 Molecular weight and intrinsic viscosity.....	83
3.3.3 Fourier-transform infrared spectroscopy.....	85

3.3.4	Mechanism of increase in molecular weight of PA66 matrix.....	86
3.3.5	Thermal decomposition .....	88
3.3.6	Crystallization .....	89
3.3.6.1	Non-Isothermal Crystallization .....	89
3.3.6.2	Isothermal Crystallization .....	91
3.4	Conclusions .....	94
	References.....	95
	Chapter 4.....	100
4	Conclusions and Recommendations for Future Study.....	100
4.1	Conclusions .....	100
4.2	Contributions .....	102
4.3	Recommendations for Future Study .....	102
	Curriculum Vitae .....	104

## List of Tables

Table 1.1 Properties of Fibers [6].	13
Table 1.2 Properties of common thermoplastic and thermoset [8].	16
Table 1.3 Properties of commonly available glass fibers [12].	22
Table 1.4 Comparison of Properties of PA6 and PA66.	26
Table 2.1 Non-isothermal crystallization data of materials collected within D-LFT process. The numbers in the parenthesis are the standard deviations ( $n = 3$ ).	61
Table 2.2 Avrami parameters of materials collected within D-LFT process. The numbers in the parenthesis are the standard deviations ( $n = 3$ ).	64
Table 3.1 Non-isothermal crystallization data of materials collected within the D-LFT process. The numbers in the parenthesis are the standard deviations ( $n \geq 3$ ).	90
Table 3.2 Avrami parameters of materials collected within the D-LFT process. The numbers in the parenthesis are the standard deviations ( $n \geq 3$ ).	93

## List of Figures

Figure 1.1 Classification of composite materials.....	12
Figure 1.2 The effect of temperature on the Elastic Modulus[6]. .....	15
Figure 1.3 Classification of the manufacturing processes for LFTs. [9].....	18
Figure 1.4 Schematic of the D-LFT Process.....	20
Figure 1.5 Chemical structure of glass. ....	21
Figure 1.6 The layered structure of carbon fiber [15]. ....	23
Figure 1.7 Chemical Structures of (a) PA6 and (b) PA66. ....	25
Figure 1.8 Mechanism of C-N bond cleavage. ....	27
Figure 1.9 Mechanism of hydrolysis and further reactions. ....	28
Figure 1.10 Mechanism of C-C bond cleavage.....	29
Figure 1.11 Mechanism of branching.....	30
Figure 1.12 Mechanism for thermo-oxidation of PA. ....	32
Figure 1.13 Oxidation of methylene group in PA.....	33
Figure 1.14 Subsequent oxidation of methylene group during PA oxidation.....	34
Figure 1.15 Mechanism of branching on carbonyl group.....	35
Figure 1.16 Azomethine polycondensation. ....	35
Figure 2.1 Schematic of D-LFT process with identified equipment as well as indicated locations for sample collection: (a) virgin, (b) first extruder, (c) second extruder, and (d) compressed plaque samples.....	45

Figure 2.2	Screw configurations of second extruder: (a) conveying screw and (b) mixing screw, where flow direction of material is from left to right. ....	48
Figure 2.3	Material discoloration throughout D-LFT process with different screw configurations. ....	53
Figure 2.4	(a) Weight-average molecular weight and (b) <i>PDI</i> of virgin, first extruder, second extruder, and compressed plaque samples processed with different screw configurations. ....	55
Figure 2.5	(a) Mark-Houwink plots and (b) $\alpha$ values obtained from Mark-Houwink plots of virgin, first extruder, second extruder, and compressed plaque samples processed with different screw configurations. ....	56
Figure 2.6	TGA curves of virgin, first extruder, second extruder, and compressed plaque samples processed with different screw configurations. ....	57
Figure 2.7	Horowitz-Metzger plots of virgin, first extruder, second extruder, and compressed plaque samples processed with different screw configurations. ....	58
Figure 2.8	Activation energy of virgin, first extruder, second extruder, and compressed plaque samples processed with different screw configurations. ....	59
Figure 2.9	Non-isothermal DSC curves of virgin, first extruder, second extruder, and compressed plaque samples processed with different screw configurations: (a) cooling curves and (b) heating curves. ....	60
Figure 2.10	Isothermal DSC curves of virgin, first extruder, second extruder, and compressed plaque samples processed with different screw configurations. ....	63
Figure 2.11	Avrami plots of virgin, first extruder, second extruder, and compressed plaque samples processed with different screw configurations. ....	63
Figure 2.12	Crystallization half-time of virgin, first extruder, second extruder, and compressed plaque samples processed with different screw configurations. ....	65

Figure 3.1	Schematic of the D-LFT process with identified equipment as well as indicated locations for sample collection: (a) virgin PA66, (b) first extruder, (c) second extruder, (d) half conveyer, and (e) compressed plaque samples. ....	74
Figure 3.2	Material discoloration throughout the D-LFT process: (a) virgin PA66, (b) first extruder, (c) second extruder, (d) half conveyer, and (e) compressed plaque samples. ....	83
Figure 3.3	(a) Weight-average molecular weight and (b) PDI of the PA66 matrix in samples collected within the D-LFT process. ....	84
Figure 3.4	(a) Mark-Houwink plots and (b) $\alpha$ values obtained from Mark-Houwink plots of the PA66 matrix in samples collected within the D-LFT process. ....	85
Figure 3.5	(a) FTIR spectra and (b) amide N-H stretching peaks of the PA66 matrix in samples collected within the D-LFT process. ....	86
Figure 3.6	Mechanism of increase in molecular weight of the PA66 matrix. ....	87
Figure 3.7	TGA curves of materials collected within the D-LFT process. ....	88
Figure 3.8	(a) Horowitz-Metzger plots of materials collected within the D-LFT process and (b) activation energy of materials collected within the D-LFT process. ....	89
Figure 3.9	Non-isothermal DSC curves of materials collected within the D-LFT process: (a) cooling curves and (b) heating curves. ....	90
Figure 3.10	Isothermal DSC curves of materials collected within the D-LFT process.	
	92	
Figure 3.11	(a) Avrami plots of materials collected within the D-LFT process and (b) crystallization half-time of materials collected within the D-LFT process. ....	92

# Chapter 1

## 1 Introduction

### 1.1. Composites

Petroleum based fossil fuels have been the key sources of energy in the transportation sector, which includes everything from automobiles to advanced jetliners. It, hence, comes as no surprise that changes in fuel costs significantly impact business models adopted by many component and equipment manufacturing companies in the market supply chain, rendering some businesses profitable while driving the others out of business. Rising fuel costs have recently forced prominent players in the commercial aviation sector like Iceland based WOW air and India registered Jet airways to cease their operations. At the same time, increasing demand in transportation sector has led to a greater consumption of fuels, further leading to environmental problems such as air pollution and global warming. This has forced governing bodies in several countries to adopt an environmentally conscious approach. Germany has set a target of reducing carbon emissions by 95% till the year 2050 (as compared to emissions in 1990) for its automobile manufacturers [1]. The Chinese government has chosen the city of Shenzhen as a pilot-site to be at the forefront of being an electrified-motor city. Furthermore, consumer trends have rapidly evolved with respect to their vehicular purchase. Henry Ford's axiom in automotive "so long as it's black" is steadily losing ground, and the consumers are getting increasingly specific and aware of the overall technical specifications (such as mileage and fuel consumption per 100 km) and aesthetics of the car. Driven by these economic, legislative and market considerations, light

weight design has become one of the core design principles in transportation industry all around the globe in the last few decades. Composite materials have emerged as a frontrunning solution to the light-weighting challenge, as they are lighter than other competitor materials such as steel and aluminum and can be tailor-made to a specific application.

Composite materials are heterogenous materials made of multiple components of dissimilar physical and chemical properties, and the final effective properties of these materials are different and an improvement over their components. Humans began exploring the use of composite material long before the word “composite” was defined. Driven by the desire to construct solid and reliable houses, stronger materials like “Wattle and Daub” were invented at least about 6000 years ago. “Wattle and Daub” is a system of walls in which a woven lattice of wooden strips called wattle is ‘daubed’ with mud fabricated with clay, sand and vegetable fibers in desired proportion [2], [3]. Nowadays, concrete, which is also composite, is the most widely used building material in the world.

Continuous efforts to improve the fuel economy have given birth to airliners such as Airbus A350 XWB and Boeing B787 series in the recent times in aviation industry. Both A350 XWB and B787 have sought solution to reduce the overall weight and carbon emissions by employing composites. The B787 uses composites for half of its airframe including the fuselage and wing, while Airbus's A350 XWB has both its fuselage and wings made of carbon fiber. But most importantly, more than 90 percent light-weighting materials are employed in automotive industry at present [4]. Automotive industry is currently the biggest market for light-weighting materials and is expected to grow at the rate of 8.8% by 2022 [5].



Composites combine two or more solid materials and can be classified as the matrix and reinforcement. The often stiffer ‘reinforcement’, which also imparts the composite its higher strength and stiffness, is dispersed or embedded into a softer ‘matrix’, which performs the tasks of keeping the reinforcement in its place, protecting it from the external environment and transferring applied external loads to the reinforcement. Based on the type, chemical nature and geometric arrangement of the constituents, composite materials may be classified as in Figure 1.1. The term ‘c’ in its contemporary sense encompasses a broad range of materials, but the discussion in this study would be limited to ‘fiber reinforced polymer composites’.

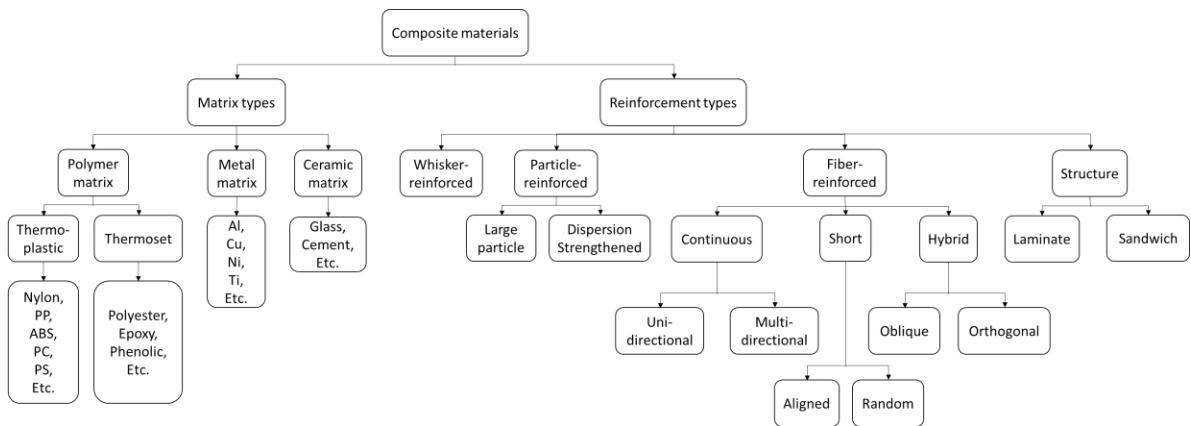


Figure 1.1 Classification of composite materials.

### 1.1.1. Reinforcement

Fiber reinforcement can be broadly classified as continuous and discontinuous fiber reinforcement. In the case of continuous fiber reinforcement, the fibers extend through the entire length of the composite [6]. UD tapes, prepregs and textile composites (such as Non-crimp fabrics, wovens, etc.) qualify as continuous fiber reinforcement. On the other hand, discontinuous fiber reinforcement comprises of chopped fibers dispersed into the matrix.

The orientation of the dispersed fibers may be random or aligned. The discontinuous fiber reinforcement can be classified as long fiber (3-50 mm) and short fiber (0.1-3 mm) by the fiber length. The fiber length must be greater than the so-called ‘critical fiber length’ for efficient strengthening and stiffening of the composite to occur. Critical fiber length ( $l_c$ ) is defined as the minimum fiber length at which maximum allowable fiber stress can be achieved [6]. The  $l_c$  is dependent upon the ultimate strength of the fiber ( $\sigma_f$ ), maximum matrix shear strength ( $\tau_m$ ) and the diameter of the fibers ( $d_f$ ), and may be calculated as:

$$l_c = \frac{\sigma_f d_f}{2\tau_m}$$

Based on source, fibers may be categorized as natural fibers and chemical fibers, which can further be grouped into inorganic fibers and organic fibers. For example, hemp fibers and jute fibers are natural fibers; aramid fibers are organic fibers; and glass fibers and carbon fibers are inorganic fibers [6]. A detailed account of glass fibers and carbon fibers will be presented further.

Table 1.1 Properties of Fibers [6].

	Density (g/cm <sup>3</sup> )	Tensile strength (GPa)	Young's modulus (GPa)	Specific modulus (E/ $\rho$ )	Specific strength ( $\sigma/\rho$ )
<b>E-Glass fiber</b>	2.54	3.5	72.4	28.5	1.38
<b>S-Glass fiber</b>	2.48	4.6	85.5	34.5	1.85
<b>Carbon fiber (high modulus)</b>	1.90	2.1	390.0	205.0	1.1
<b>Carbon fiber (high modulus)</b>	1.90	2.5	240.0	126.0	1.3
<b>Kevlar 49 (aramid polymer)</b>	1.50	2.8	130.0	87.0	1.87

### 1.1.2. Matrix

Polymers are classified as thermoset and thermoplastic based on intermolecular forces [6]. The thermoset polymer chains are connected by strong covalent chemical cross-links, leading to a rigid 3D structure. These irreversible chemical bonds impart high temperature resistance, but also render the thermoset single-use. Whereas in thermoplastic polymers, chains are entangled and held together by weak secondary forces (such as van der Waals forces). These chains tend to disentangle when heated beyond the glass transition temperature, transiting from a brittle glassy state to a softer rubbery state. Thermoplastics, therefore, can easily be reshaped and recycled. Based on the degree of crystallinity, thermoplastics may be further classified as semi-crystalline and amorphous. Amorphous polymers exhibit a short-range ordering, or in other words, the polymer chains are randomly arranged. On the other hand, semi-crystalline polymers show regions of long-range ordering, in which polymer chains are packed in a uniform repetitive pattern, along with amorphous regions. As can be seen in Figure 1.2, amorphous polymers exhibit a transition from a glassy state to a rubbery state over glass transition temperature (due to chain disentanglement, as discussed before) before they eventually melt, whereas the semi-crystalline polymers show a sharp melting point.

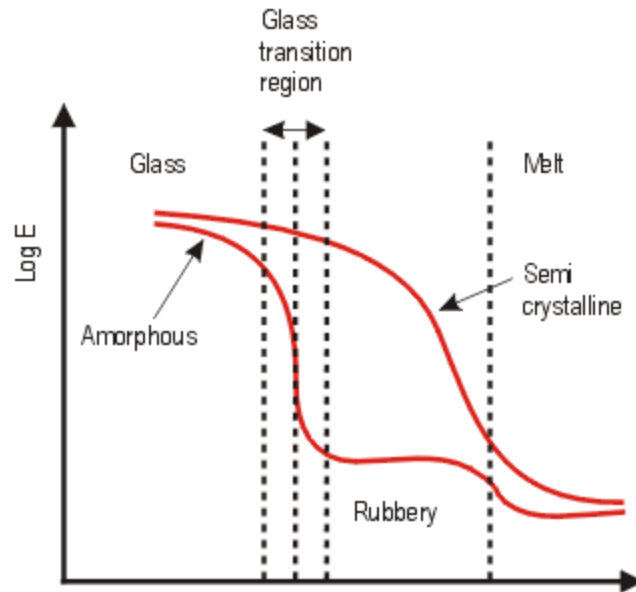


Figure 1.2 The effect of temperature on the Elastic Modulus [6].

The mechanical properties of the polymer matrix are highly dependent on their microstructure. When a load is applied, a thermoset polymer fails due to scission of the bonds forming their rigid 3D structure. The molecular chains of thermoplastics, on the other hand, begin to get drawn out of the entangled mix and orient themselves in the direction of loading.

Examples of thermosets include epoxy, silicone, polyurethane and phenolics. Polyethylene, and examples of thermoplastics are polypropylene, polystyrene, nylon and Teflon [7]. Some of their  $\alpha$  have been tabulated below (Table 1.2).

Table 1.2 Properties of common thermoplastic and thermoset [8].

	Tensile strength (MPa)	Young's modulus (GPa)	Maximum strain (%)	Maximum operation temperature (°C)
Unsaturated polyester	50-70	3.5-4.7	2-5	100
Epoxy	70-90	2.8-3.7	2-10	200
Phenol	15-20	3.5-5.9	1-2	250
Polypropylene (PP)	25-40	1.0-2.0	100-600	80
Polyamide (PA)	80-90	3.0-3.2	70-300	100
Polyether ether ketone (PEEK)	100-120	3.6-3.8	80-100	250

### 1.1.3. Reinforcement-matrix Interface

When a load is applied on fiber reinforced polymer composites, the stress is transferred from the matrix to the fibers through the fiber-matrix interface. An efficient stress transfer makes composites capable of achieving higher modulus and strength [6]. The quality of the interface is, hence, an important characteristic of composites. Quality of interface depends on the wettability (the tendency of a liquid to spread over a solid surface) and bonding between fibers and a polymer matrix. A higher wettability of a polymer matrix over fiber surface is desired, as that would be expected to lead to minimizing flaws such as voids at the interface. The wettability may be improved by using a polymer matrix that has a low viscosity and applying a high pressure on the interface during processing. The interfacial bond, on the other hand, may be enhanced by chemical bonds, chain

entanglements, or electrostatic attraction between fibers and a matrix. Roughening fiber surface may also promote mechanical interlocking [6], [8].

## 1.2. Background

### 1.2.1. Long-fiber Reinforced Thermoplastics

The market for long-fiber reinforced thermoplastics (LFTs) has grown rapidly over the past 30 years. As the name implies, the composites include long fibers, which increase mechanical properties of thermoplastics effectively. In addition, since the matrix is a thermoplastic, the composites have good productivity (short cycle time) and recyclability. Manufacturing techniques for LFTs have become increasingly sophisticated and reliable for mass production of high-quality parts for structural applications [9].

### 1.2.2. Processing Techniques

Manufacturing techniques for LFTs is summarized in Figure 1.3, along with information on corresponding commercial products in italics [9].

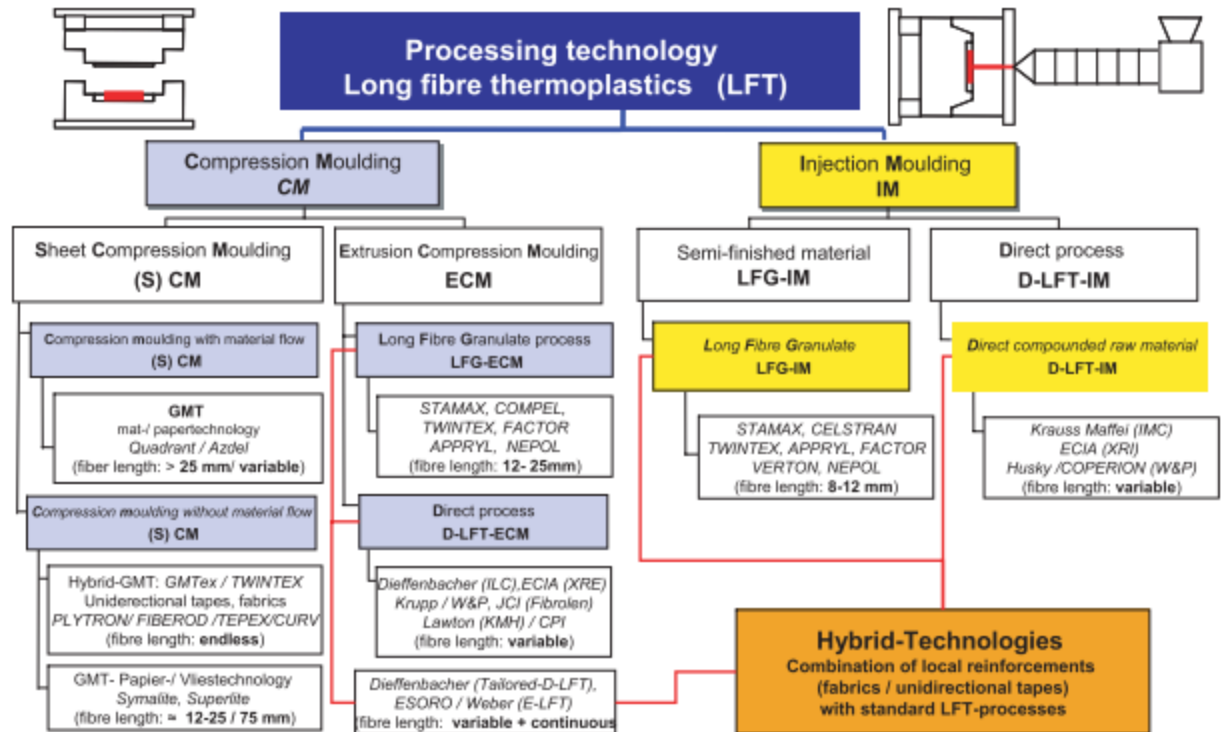


Figure 1.3 Classification of the manufacturing processes for LFTs [9].

Glass mat thermoplastic (GMT) was the most popular process for LFTs in the past, and was widely used for parts with simple geometry such as covers in automobile industry [9]. In this technique, long-fiber mats with a random fiber orientation are consolidated with thermoplastic sheets. Although GMT products are stiff and tough, they were more expensive than the injection molded thermoplastics. Furthermore, glass bridging, which creates resin-rich areas, was identified as a challenge in GMTs [10].

Long fiber reinforced thermoplastic granulates (LFT-G) later emerged as another popular process. In this technique, pellets with long fibers are first prepared using wire coating, crosshead extrusion or pultrusion. The pellets (or long fiber granulates) are then molded using injection molding (IM), injection compression molding (ICM) or extrusion

compression molding (ECM). However, fibers with initial fiber length over 13 mm were found to be broken and in some cases, jammed in the equipment such as a nozzle [9], [11].

The Direct long-fiber reinforced thermoplastics (D-LFT) process was developed in the late 90s to manufacture cost-effective LFT products. The D-LFT combines compounding and compression molding of LFTs into one process and skipped a step to make semi-finished products [7]. The process is shown in Figure 1.4, The D-LFT line consists of a dryer, two extruders, a conveyor and hydraulic press. The thermoplastic pellets are first dried using the dryer. The dried pellets are then fed gravimetrically into the first extruder through the hopper. The thermoplastic melts in the first extruder and is fed into the second extruder. The fibers from the roving are then fed into the second extruder. The fibers are mixed with the thermoplastic melt and chopped due to the action of the screws. The molten composite, called plastificate, is cut to desired dimensions and transported to the hydraulic press using the conveyor. The plastificate is then compressed to shape a final product using the press.



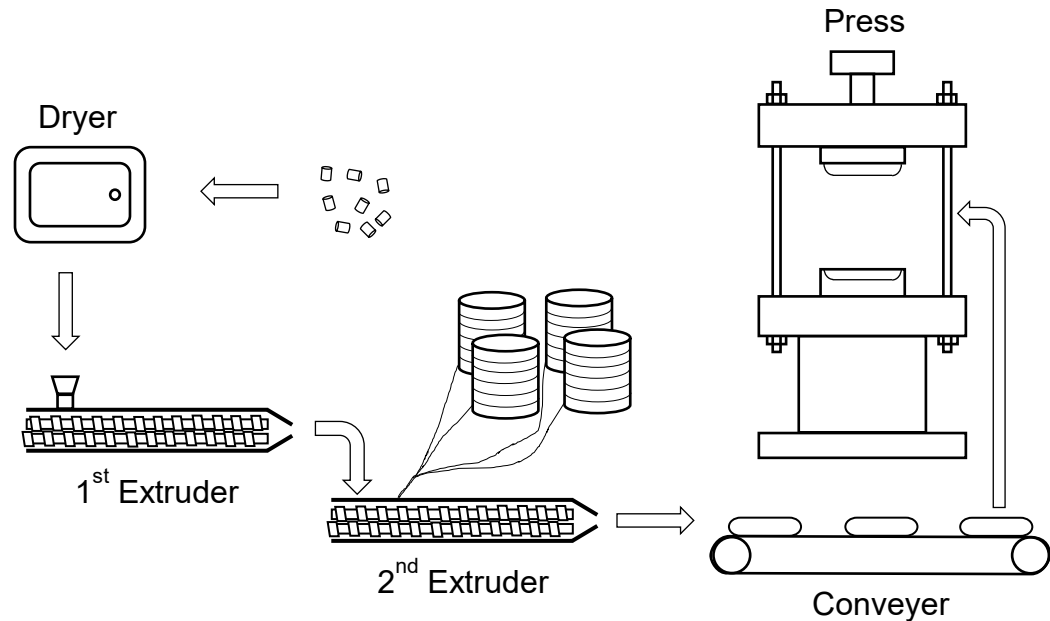


Figure 1.4 Schematic of the D-LFT Process.

### 1.2.3. Candidate Materials for D-LFT Process

#### 1.2.3.1. Fibers

##### 1.2.3.1.1. Glass Fibers

Glass fibers are one of the most primary reinforcements in composites due to their high performance-to-cost ratio and a ready availability. Advantages of glass fibers are good heat resistance, chemical resistance, and mechanical properties such as hardness, strength and modulus, which makes them a favourable choice as a reinforcement. Continuous glass fibers are produced by directly extruding the molten glass through bushings containing thousands of orifices. The bushings are made of corrosion resistant metals, such as platinum alloys, and the diameter of the fibers can be controlled by controlling the diameter of orifices [12].

Glass fibers can be made from silica ( $\text{SiO}_2$ ) and various types of oxides such as aluminium oxide, calcium oxide, boron oxide, etc.[12] At a molecular level, glass fibres consist of silicon and oxygen covalently bonded in a rigid 3-D tetrahedral structure, where the silicon atoms are located at the center and the oxygen atoms are at the corners. This leads to isotropic properties.

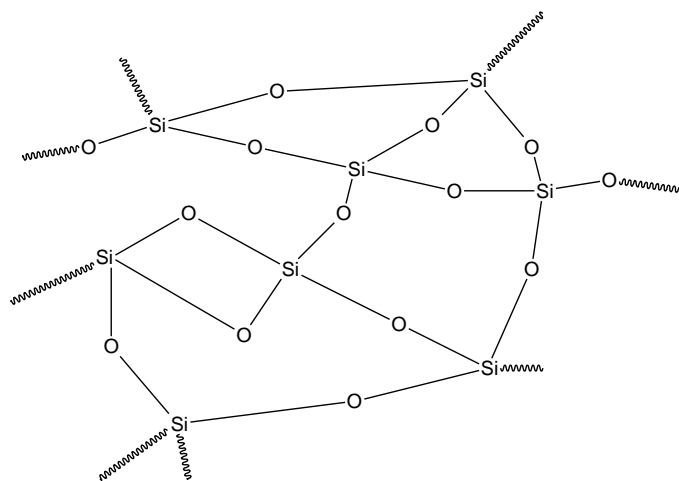


Figure 1.5 Chemical structure of glass.

Glass fibers are commercially available as either low-cost general-purpose glass fibers, commonly known as E-glass, or as premium special-purpose fibers. E-glass fibers hold a 90% share of the glass fiber market. E-glass fibers are generically available with about 4-5 wt% boron oxide, or in an environmentally friendly boron oxide free variant. Boron oxide is primarily added to make the softening temperature of E-glass distinct. On the other hand, premium special-purpose glass fibers are utilized for their unique properties to cater to specific applications. S-glass, C-glass and D-glass are a few examples of such special-purpose fibers. Their alphabetic designations are indicative of their unique characteristics. For example, 'S' in 'S-glass' refers to high strength, 'C' in 'C-glass' refers

to high chemical durability, ‘D’ in ‘D-glass’ indicates a low dielectric constant, etc.[12]

Table 1.3 summarizes key properties of some commercially available glass fiber variants.

Table 1.3 Properties of commonly available glass fibers [12].

	Density (g/cm <sup>3</sup> )	Liquidus Temperat ure (°C)	Softening Temperat ure (°C)	Specific Heat (cal/g/°C)	Tensile strength at 23 °C (MPa)	Young’s modulus (GPa)	Specific modulus (E/ρ)	Specific strength (σ/ρ)
<b>Boron- containing E-Glass</b>	2.54-	1006-1700	830-860	0.192	3100-3800	76-78	29.80-	1215.69-
	2.55						30.71	1496.06
<b>Boron-free E-Glass</b>	2.62	1200	916		3100-3800	80-81	30.53-	1183.21-
							30.92	1450.38
<b>ECR-Glass (Electrical/ Chemical Resistance)</b>	2.66-	1159	880		3100-3800	80-81	29.85-	1156.72-
	2.68						30.45	1428.57
<b>D-Glass</b>	2.16		770	0.175	2410			1115.74
<b>S-Glass</b>	2.48-	1500	1056	0.176	4380-4590	88-91	35.34-	1759.04-
	2.49						36.69	1850.81

### 1.2.3.1.2. Carbon Fibers

Carbon fibers have been expanding their application areas owing to increasing demands for high-performance-lightweight materials across various sectors such as transportation, energy, sports, etc. and recent improvements in the processing techniques with respect to cycle times and production costs. Carbon fibers have a high strength to weight ratio and low thermal expansion co-efficient. They are also stable at higher temperatures, resistant to chemicals, and electrically conductive.

Carbon fibers have paracrystalline and layered graphitic structures. Carbon atoms are arranged in a hexagonal lattice (forming sheets of graphene), which are stacked in an ABAB... sequence in a single graphite unit cell, as shown in Figure 1.6. The fibers may be formed by either folding these graphene sheets or by rolling them concentrically with increasing radii. The strong covalent bonds between carbon atoms in the graphene lead to superior mechanical properties, when subjected to in-plane axial loading. The graphene sheets, however, are held together only by weak Van Der Waals' forces, leading to inferior properties in in-plane transverse or radial directions. The graphitic structure of the carbon fiber, hence, makes it highly anisotropic [13], [14].

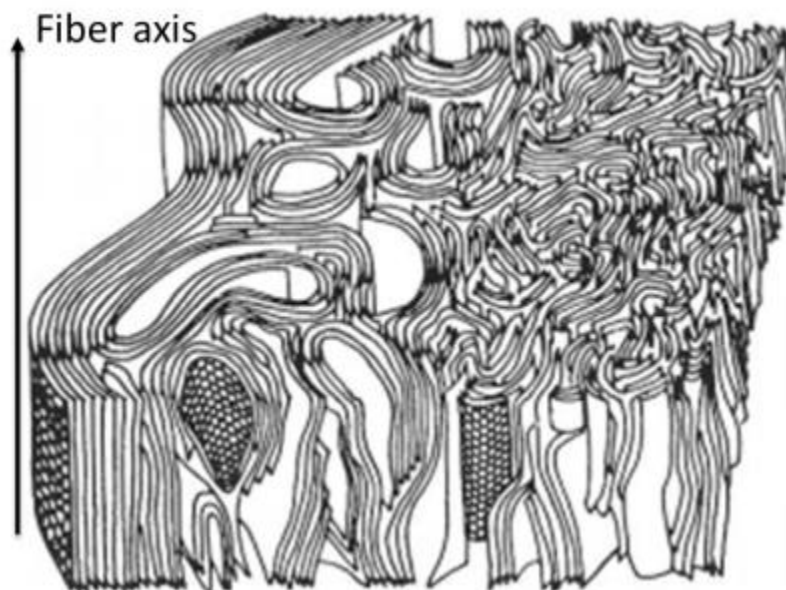


Figure 1.6 The layered structure of carbon fiber [15].

Carbon fibers are commercially available as either general-purpose (GP) fibers, high performance (HP) fibers, or activated carbon (ACF) fibers. Although low-cost, GP fibers has low strength and modulus as compared to HP fibers. While GP fibers find their

application as a reinforcement in concrete and as sealing materials, fillers, etc., HP fibers and HP fiber based composites find applications as structural components in aerospace and automotive industries. ACF fibers, on the other hand, have a high micropore volume and are used for adsorption. Carbon fibers may also be classified based on degree of graphitization as: ultrahigh modulus (UHM), high modulus (HM), intermediate modulus (IM), high tensile strength (HT) and isotropic carbon fibers [6], [8], [13], [14]. UHM and HM possess high modulus, whereas IM and HT have low modulus but high strength. Isotropic fibers have low strength and modulus, as they just comprise of randomly oriented graphitic crystallites [13], [14].

### 1.2.3.1. Matrix

#### 1.2.3.1.1. Polyamides

Polyamides (PAs), also known as “Nylons”, were first commercialized by DuPont with the goal of capturing the newly emerging synthetic fibers market in the late 1930s. The name “Nylon” was the trade name initially used by DuPont, but then eventually evolved as an identity for the class of thermoplastic polyamides [16]. Recently, PAs have emerged as a candidate for the matrix of fiber reinforced thermoplastics due to their excellent properties such as good toughness, impact resistance, abrasion resistance, lubricity and resistance to organic solvents [16]–[20].

Commercial PAs are manufactured using three methods. The first method involves polycondensation reaction between diamines and diacids. PA66 is a product of such a

polycondensation reaction. The first number in the name refers to the number of carbon atoms in the diamine, the second number is the number in the diacid. The second method is opening a monomer containing both amine and acid groups, which is known as a lactam ring. In this case, the PA identity is based on the number of carbon atoms in the lactam monomer (e.g., PA6). The third method is polycondensation of  $\omega$ -amino acids. PA 11, formed by 11-aminoundecanoic acid, is synthesized using this method[21].

### 1.2.3.1.2. Polyamide 6 and Polyamide 66

PA6 and PA66 are most widely used PAs as engineering plastics. Their chemical structures are shown in Figure 1.7.

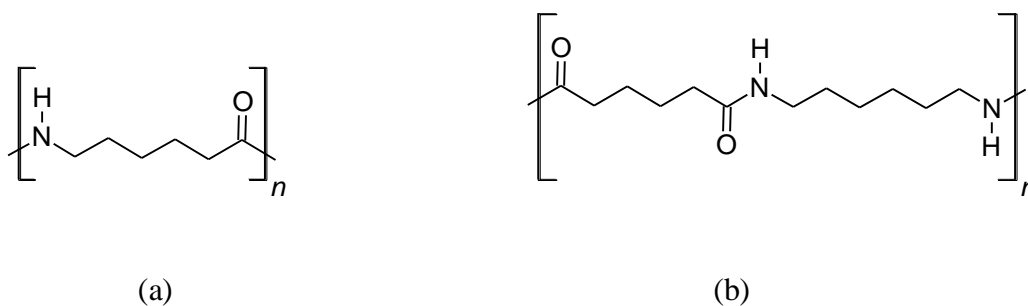


Figure 1.7 Chemical Structures of (a) PA6 and (b) PA66.

PA66 has higher modulus and absorbs less water than PA6. Furthermore, PA66 shows higher melting, glass transition, and deflection temperatures than PA6. The higher heat deflection temperature and lower moisture absorption of PA66 allow for improved performance in applications where integrity at higher temperature and moist conditions is desired. Additionally, high modulus of PA66 is ideal for applications that demand

structural, chemical and thermal integrity [16]–[20]. Table 1.4 compares properties of PA6 and PA66.

Table 1.4 Comparison of Properties of PA6 and PA66.

	PA6	PA66
Mechanical Properties	Higher impact energy	Higher tensile modulus
	Higher strength	Higher flexural modulus
Crystallinity	Low	High
Water absorption rate	Slightly higher than PA66	Slightly lower than PA6 but still moisture sensitive
Hydrocarbon resistance	Higher	Lower
Heat deflection temperature	Lower	Higher
Melting temperature	Lower (220°C)	Higher (264°C)
Mold shrinkage	Less	Greater
Processability	Easier to process due to lower melting temperature	More challenging to process due to higher melting temperature
		Reddish-brown tinting when produced
		More difficult to color

#### 1.2.3.1.3. Possible Reactions Through D-LFT Process

A polymer matrix is processed under heat and oxidation during the D-LFT process. Therefore, chemical reactions may occur in the polymer matrix and change molecular





Hydrolysis is another reaction for chain scission. Hydrolysis of an amide by water leads to formation of a ketone, carbon dioxide, ammonia, and water, as shown in reactions in Figure 1.9 [16], [22], [23], [25]. Hydrolytic scission of a peptide bond was believed to be the mechanism responsible for high CO<sub>2</sub> concentration [16], [22], [23], [25].

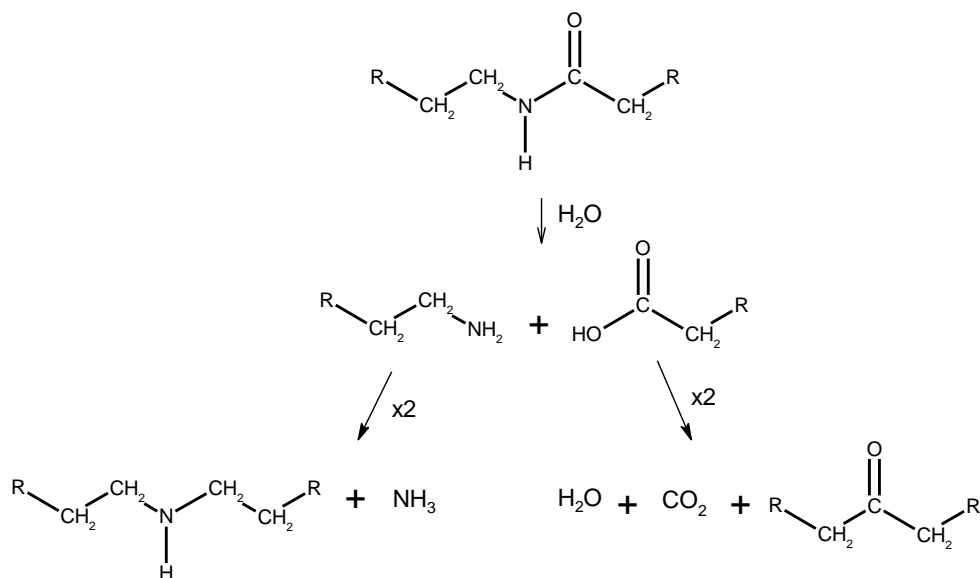


Figure 1.9 Mechanism of hydrolysis and further reactions.

Cleavage of a N-alkylamide bond or CH<sub>2</sub>-CH<sub>2</sub> linkage between alpha-position and beta-position of carbonyl group has been identified as a competing reaction mechanism to the primary homolytic C-N bond scission at high temperatures, which forms lower molecular weight hydrocarbon fragments (Figure 1.10) [16], [25].

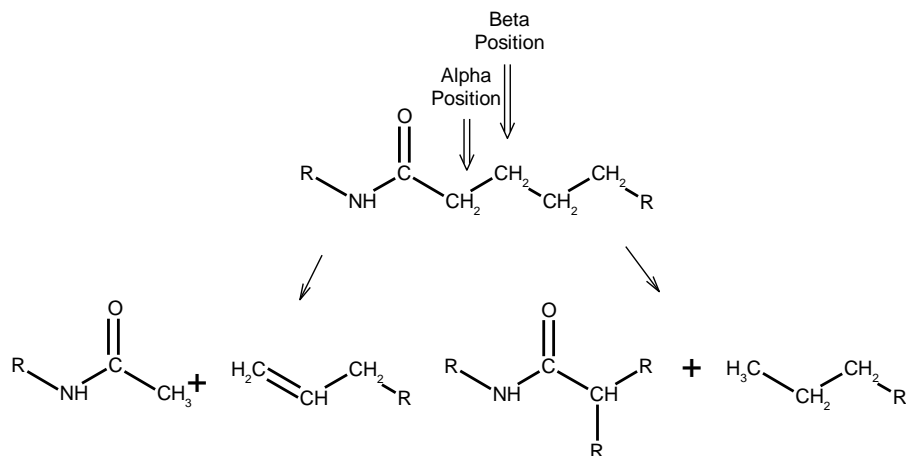


Figure 1.10 Mechanism of C-C bond cleavage.

Unlike PA6, there is no agreement on which bond would undergo a preferential scission at low or moderate temperatures in PA66. CH<sub>2</sub>-CH<sub>2</sub>, CH<sub>2</sub>-NH, C-H, and CO-CH<sub>2</sub> bonds have all been reported as likely candidates for scission [16].

### 1.2.3.1.3.1.2. Branching

Branching of PA molecules can occur at high temperature. Carbonyl and secondary amide group are formed by condensation of two acids, and two amines, respectively. These groups act as sites for branching in amines. Expected branching mechanisms with carbonyl and secondary amine groups are shown in Figure 1.11 [16], [22], [23], [25], [26].

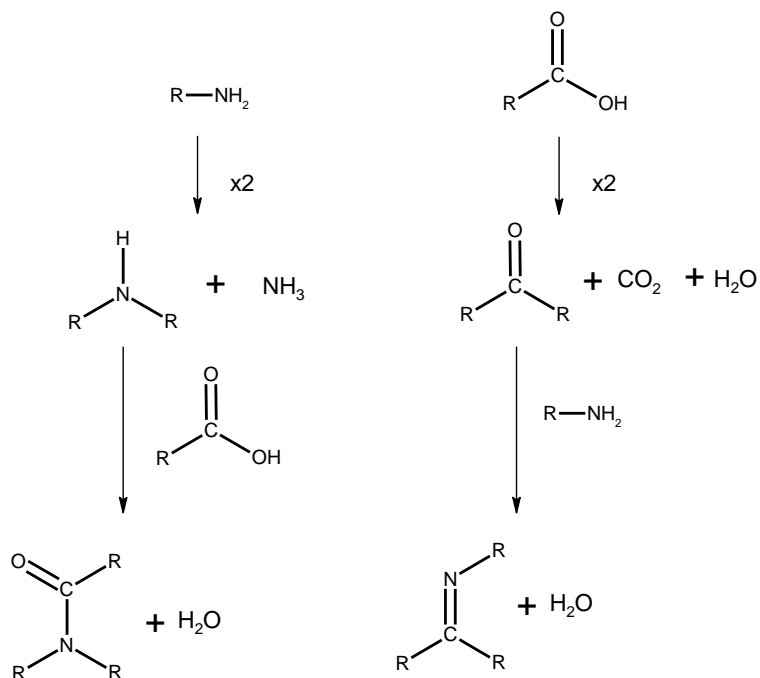


Figure 1.11 Mechanism of branching.

### 1.2.3.1.3.2. Thermal Oxidation Reaction

#### 1.2.3.1.3.2.1. Chain Scission

With participation of oxygen, new degradation mechanisms have been proposed. Three possible overall reactions have been proposed in the initial studies on oxidation of polyamides [16]:

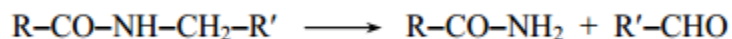
- (i) Formation of N-acylamide (imides):



- (ii) Formation of N-formamides (formimidies) due to the scission of CH<sub>2</sub>-R' bond:



(iii) Formation of carbonyl compounds via oxidative dealkylation:



Removal of hydrogen atom from the N-vicinal methylene group and oxidation of the macroradical were found to be the initiation and propagation mechanisms of thermal oxidation in their studies. Experimental evidence supported the initiation of thermal oxidation by attack of oxygen on the N-vicinal methylene group, as homologous aliphatic normal monocarboxylic, dicarboxylic, valeric acid and adipic acid were found to be the main thermo-oxidation products [16].

A revised mechanism, including chain scission, for thermo-oxidation of PAs has been proposed. As described above, primary reactions occur on the N-vicinal methylene group, which was backed by several other authors [16], [22], [26], [27]. A newly formed radical on the N-vicinal methylene group reacts with oxygen, and a new radical is formed, which may then either isomerize or form carbonyl- or carboxyl end group containing compounds, as shown in Figure 1.12.

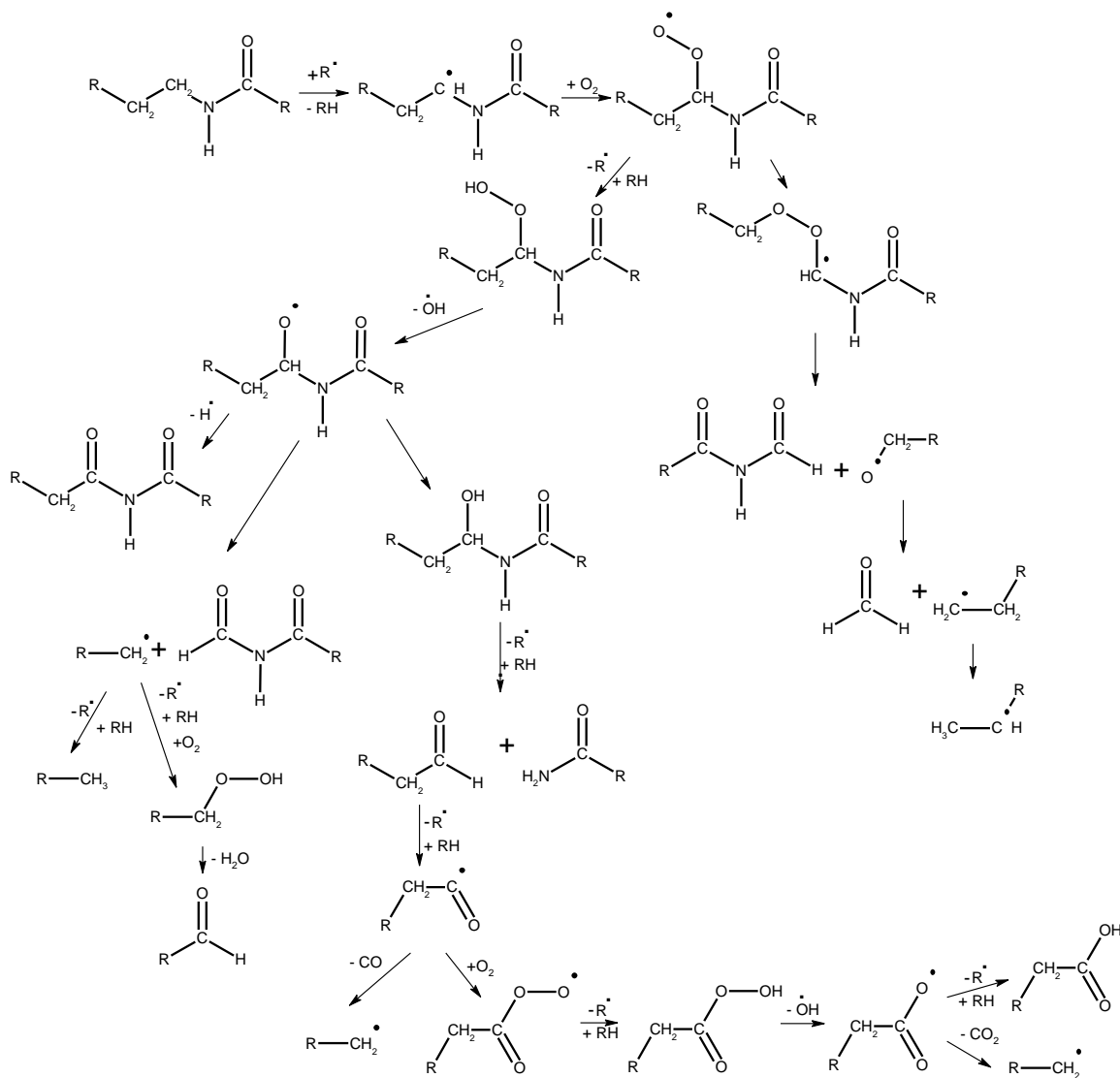


Figure 1.12 Mechanism for thermo-oxidation of PA.

Formation of a carbonyl compound and a free macroradical via beta-scission of other methylene group during oxidation has also been reported for PAs [16]. Figure 1.13 shows the suggested mechanism.

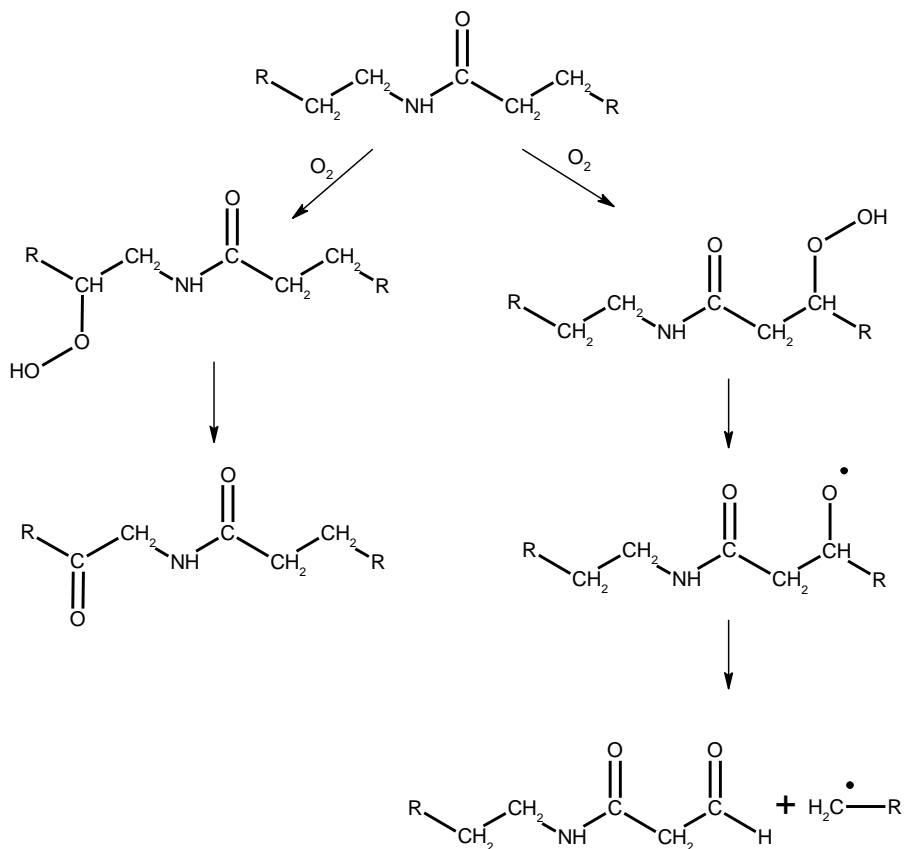


Figure 1.13 Oxidation of methylene group in PA

Further oxidation of methylene group post formation of N-acylamides has been supported by a number of research groups (Figure 1.14) [16]. Either degradation of N-acylamide into cyano and carboxyl group or further oxidation of N-acylamide group to a  $\alpha, \beta$ -unsaturated carbonyl has been suggested.  $\alpha$ -methylene group has also been considered as a likely site for preferential oxidation.

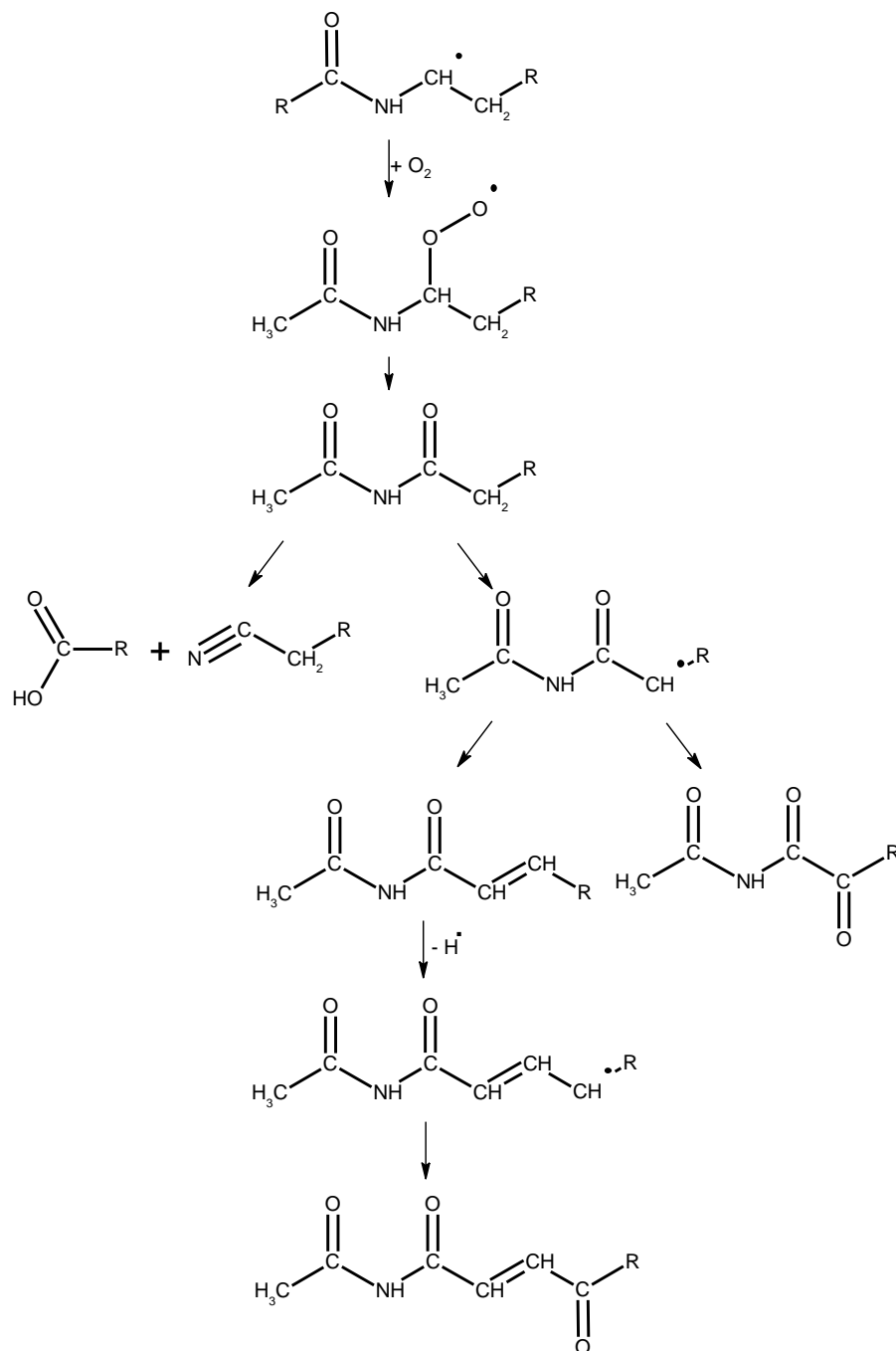


Figure 1.14 Subsequent oxidation of methylene group during PA oxidation.

### 1.2.3.1.3.2.2. Branching

Branching may occur through a reaction between an amine end group and a carbonyl group in PA, which may be formed by thermo-oxidation mentioned above, as shown in Figure 1.15 [16], [22], [23], [25]–[27].

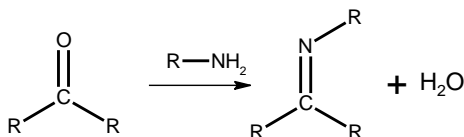


Figure 1.15 Mechanism of branching on carbonyl group.

Azomethine polycondensation may also cause branching in PAs. The working principle is consumption and regeneration of amine end groups by azomethine condensation reaction (Figure 1.16) [16]. This exchange of amine groups is occurred at higher temperatures.

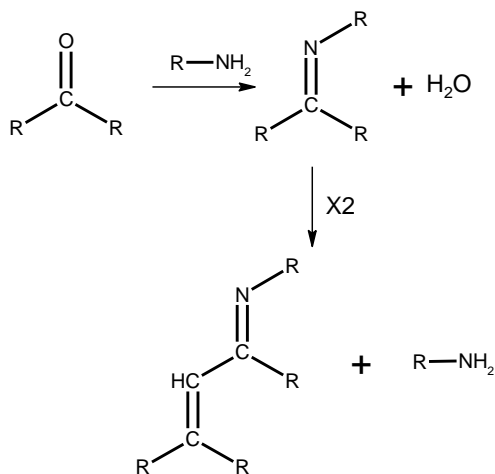


Figure 1.16 Azomethine polycondensation.



### 1.3. Research Background

Mechanical and thermal properties of various types of PA-based composite materials, such as glass fiber/PA, carbon fiber/PA, carbon nanotube/PA, and graphene/PA, were studied in the past [28]–[37]. The PA-based composite materials reported in these studies were manufactured mostly through an injection molding, GMT, and vacuum-assisted resin transfer molding (VARTM) [29],[38],[39]. Since processing techniques have effects on properties of the composite materials [40], it is essential to study properties of PA-based composite materials manufactured through the D-LFT process. Whitfield et al. [41] studied the effects of extruder temperature and screw speed on the thermal properties of glass fiber reinforced PA6 composites in the D-LFT process. The molecular weight of the PA6 matrix was found to decrease at the high extruder temperature and low screw speed. However, the high extruder temperature and low screw speed increased activation energy for decomposition. While the extruder temperature and screw speed had little effect on the degree of crystallinity, the low screw speed increased crystallization half-time.

### 1.4. Objectives

PA-based composite materials manufactured through the D-LFT process are good candidates to be used for products where mechanical and thermal loadings are exerted. The main objective of this study is to investigate the thermal properties of PA-based composite materials manufactured through the D-LFT process. Specific work includes:

- (1) Characterizing molecular weight and thermal properties of glass fiber reinforced PA6 composites at consecutive process stages within the D-LFT process, where screw configuration in the extruder is changed.
- (2) Characterizing molecular weight and thermal properties of carbon fiber reinforced PA66 composites at consecutive process stages within the D-LFT process.

## 1.5. Significance

Only a few studies have yet reported on molecular weight and thermal properties of PA based composite materials through the D-LFT process. No study has reported on how screw configuration in the extruder affects their molecular weight and thermal properties in the D-LTF process. This study investigates the effects. In addition, this study characterizes molecular weight and thermal properties of a new D-LFT product, carbon fiber reinforced PA66, which is designed to further improve performance of D-LFT products.

## References

- [1] “Climate Action in Figures: Emission Targets Germany and EU,” *Federal Ministry for the Environment, Nature Conservation, Building and Nuclear Safety*, p. 1, 2017.
- [2] T. Graham, “Wattle and Daub : Craft , Conservation and Wiltshire Case Study,” University of Bath, 2004.
- [3] G. Cuitiño, G. Maldonado, and A. Esteves, “Analysis of the Mechanical Behavior of Prefabricated Wattle and Daub Walls,” *Int. J. Archit. Eng. Constr.*, vol. 3, no. 4, pp. 235–246, 2015.
- [4] R. Heuss, N. Müller, W. van Sintern, A. Starke, A. Tschiesner, W. Van Sintern, A. Starke, A. Tschiesner, W. van Sintern, A. Starke, and A. Tschiesner, “Lightweight, heavy impact,” *McKinsey Co.*, p. 24, 2012.
- [5] “Global automotive composites market to increase at a CAGR of 8.8% by 2022,” *CompositesWorld*, 2015. [Online]. Available: <https://www.compositesworld.com/news/global-automotive-composites-market-to-increase-at-a-cagr-of-88-by-2022>. [Accessed: 27-Jun-2016].
- [6] B. D. Agarwal, L. J. Broutman, and K. Chandrashekhara, *Analysis and Performance of Fiber Composites*, 3rd ed. Hoboken, NJ, USA: John Wiley & Sons, Inc., 2006.
- [7] U. K. Vaidya and K. K. Chawla, “Processing of fibre reinforced thermoplastic composites,” *Int. Mater. Rev.*, vol. 53, no. 4, pp. 185–218, 2008.

- [8] T. Clyne and D. Hull, *An introduction to composite materials*, 3rd ed. New York, USA: Cambridge university press, 2019.
- [9] M. Schemme, "LFT – development status and perspectives," *Reinf. Plast.*, vol. 52, no. 1, pp. 32–39, Jan. 2008.
- [10] "Evolution of tailored D-LFT," *CompositesWord*, 2013. [Online]. Available: <https://www.compositesworld.com/articles/evolution-of-tailored-d-lft>. [Accessed: 24-May-2019].
- [11] F. Henning, H. Ernst, R. Brüssel, G. Co, O. Geiger, W. Krause, and F. Institut, "LFTs for automotive applications," *Reinf. Plast.*, vol. 49, no. 2, pp. 24–33, 2005.
- [12] F. T. Wallenberger, J. C. Watson, and H. Li, "Glass Fibers," *Composites*, vol. 21, no. 1, p. 0, Jan. 2001.
- [13] S. Chand, "Review Carbon fibers for composites," *J. Mater. Sci.*, vol. 35, no. 6, pp. 1303–1313, 2000.
- [14] S. Park, *Carbon Fibers*. Dordrecht, Netherlands: Springer, 2015.
- [15] S. C. Bennett and D. J. Johnson, "Structural heterogeneity in carbon fibers," 1978.
- [16] S. V Levchik, E. D. Weil, and M. Lewin, "Thermal decomposition of aliphatic nylons," *Polym. Int.*, vol. 48, no. 7, pp. 532–557, 1999.
- [17] S. M. Aharoni, *n-Nylons: their synthesis, structure and properties*. Chichester, England: John Wiley & Sons Ltd, 1997.

- [18] J. Brandrup, E. H. Immergut, and E. A. Grulke, Eds., *Polymer handbook*, 4th ed. New York, USA: John Wiley & Sons, Inc., 1999.
- [19] F. Chavarria and D. R. Paul, "Comparison of nanocomposites based on nylon 6 and nylon 66," *Polymer (Guildf)*., vol. 45, no. 25, pp. 8501–8515, 2004.
- [20] F. Faridirad, S. Ahmadi, and M. Barmar, "Polyamide/Carbon Nanoparticles Nanocomposites: A Review," *Polym. Eng. Sci.*, vol. 57, no. 5, pp. 475–494, May 2017.
- [21] C. Silva, A. M. Cavaco-Paulo, and J. J. Fu, "5 - Enzymatic biofinishes for synthetic textiles," in *Woodhead Publishing Series in Textiles*, R. B. T.-F. F. for T. Paul, Ed. Woodhead Publishing, 2015, pp. 153–191.
- [22] A. L. Bhuiyan, "Some aspects of the thermal stability action of the structure in aliphatic polyamides and polyacrylamides," *Polymer (Guildf)*., vol. 25, no. 12, pp. 1699–1710, 1984.
- [23] S. V Levchik, L. Costa, and G. Camino, "Effect of the fire-retardant, ammonium polyphosphate, on the thermal decomposition of aliphatic polyamides: Part II—polyamide 6," *Polym. Degrad. Stab.*, vol. 36, no. 3, pp. 229–237, 1992.
- [24] S. V. Levchik, G. F. Levchik, A. I. Balabanovich, G. Camino, and L. Costa, "Mechanistic study of combustion performance and thermal decomposition behaviour of nylon 6 with added halogen-free fire retardants," *Polym. Degrad. Stab.*, vol. 54, no. 2–3, pp. 217–222, Nov. 1996.

- [25] P. R. Hornsby, J. Wang, R. Rother, G. Jackson, G. Wilkinson, and K. Cossick, "Thermal decomposition behaviour of polyamide fire-retardant compositions containing magnesium hydroxide filler," *Polym. Degrad. Stab.*, vol. 51, no. 3, pp. 235–249, 1996.
- [26] T. Karstens and V. Rossbach, "Thermo-oxidative degradation of polyamide 6 and 6,6. Kinetics of the formation and inhibition of UV/VIS-active chromophores," *Die Makromol. Chemie*, vol. 190, no. 12, pp. 3033–3053, Jun. 1989.
- [27] P. Marechal, R. Legras, and J. M. Dekoninck, "Postcondensation and oxidation processes in molten polyamide 6," *J. Polym. Sci. Part A Polym. Chem.*, vol. 31, no. 8, pp. 2057–2067, Jun. 1993.
- [28] Y. Fan, Y. C. Liu, T. Whitfield, T. Kuboki, J. T. Wood, and V. Ugresic, "Effects of Processing Parameters on the Thermal and Mechanical Properties of LFT- D-ECM Glass Fiber/Polyamide 6 Composites," *Plast. Eng.*, vol. 73, pp. 44–45, Jan. 2017.
- [29] A. Hassan, N. M. Salleh, R. Yahya, and M. R. K. Sheikh, "Fiber length, thermal, mechanical, and dynamic mechanical properties of injection-molded glass-fiber/polyamide 6,6: plasticization effect," *J. Reinf. Plast. Compos.*, vol. 30, no. 6, pp. 488–498, Mar. 2011.
- [30] X. Gabrion, V. Placet, F. Trivaudey, and L. Boubakar, "About the thermomechanical behaviour of a carbon fibre reinforced high-temperature thermoplastic composite," *Compos. Part B Eng.*, vol. 95, pp. 386–394, 2016.

- [31] E. C. Botelho, Ł. Figiel, M. C. Rezende, and B. Lauke, “Mechanical behavior of carbon fiber reinforced polyamide composites,” *Compos. Sci. Technol.*, vol. 63, no. 13, pp. 1843–1855, 2003.
- [32] S. Chatterjee, F. A. Nüesch, and B. T. T. Chu, “Comparing carbon nanotubes and graphene nanoplatelets as reinforcements in polyamide 12 composites,” *Nanotechnology*, vol. 22, no. 27, p. 275714, 2011.
- [33] Liu, I. Y. Phang, L. Shen, S. Y. Chow, and W.-D. Zhang, “Morphology and Mechanical Properties of Multiwalled Carbon Nanotubes Reinforced Nylon-6 Composites,” *Macromolecules*, vol. 37, no. 19, pp. 7214–7222, Sep. 2004.
- [34] K. Soygun, G. Bolayir, and A. Boztug, “Mechanical and thermal properties of polyamide versus reinforced PMMA denture base materials,” *J Adv Prosthodont*, vol. 5, no. 2, pp. 153–160, May 2013.
- [35] W. Jie, L. Yubao, C. Weiqun, and Z. yi, “A study on nano-composite of hydroxyapatite and polyamide,” *J. Mater. Sci.*, vol. 38, no. 15, pp. 3303–3306, 2003.
- [36] X. Liu, X.-Y. Shao, L.-Y. Wang, H.-F. He, and G.-B. Fang, “Thermal stability and mechanical properties of solution mixing–processed co-polyamide–graphene composites at extremely low graphene loading,” *High Perform. Polym.*, vol. 30, no. 1, pp. 16–23, Oct. 2016.
- [37] Z. Xu and C. Gao, “In situ Polymerization Approach to Graphene-Reinforced Nylon-6 Composites,” *Macromolecules*, vol. 43, no. 16, pp. 6716–6723, Aug.

2010.

- [38] J. Karger-Kocsis, T. Harmia, and T. Czigány, “Comparison of the fracture and failure behavior of polypropylene composites reinforced by long glass fibers and by glass mats,” *Compos. Sci. Technol.*, vol. 54, no. 3, pp. 287–298, 1995.
- [39] J. P. Anderson, A. J. Kelly, and M. Altan, *Fabrication of Composite Laminates by Vacuum-Assisted Resin Transfer Molding Augmented with an Inflatable Bladder*, vol. 2. 2013.
- [40] M. T. Albdiry, B. F. Yousif, H. Ku, and K. T. Lau, “A critical review on the manufacturing processes in relation to the properties of nanoclay/polymer composites,” *J. Compos. Mater.*, vol. 47, no. 9, pp. 1093–1115, Jun. 2012.
- [41] T. Whitfield, T. Kuboki, J. Wood, V. Ugresic, S. Sathyanarayana, and K. Dagnon, “Effects of process parameters on thermal properties of glass fiber reinforced polyamide 6 composites throughout the direct long-fiber-reinforced thermoplastics process,” *Polym. Eng. Sci.*, vol. 58, no. S1, pp. E114–E123, May 2018.



## Chapter 2

# 2 Effects of Extruder Screw Configurations on Thermal Properties of Glass Fiber-Reinforced Polyamide 6 Composites throughout the Direct Long-Fiber-Reinforced Thermoplastics Process

## 2.1. Introduction

Long-fiber reinforced thermoplastics (LFT) have been attracting much attention due to their high strength-to-weight ratio, high productivity, and recyclability [1]. The manufacturing technique for LFT has been improved and made industry-scale productions a reality [2]. Glass mat thermoplastic (GMT) and long-fiber reinforced thermoplastic granules (LFT-G) are two popular techniques to produce LFT [1]-[3]. However, both GMT and LFT-G involve semi-finished products in the process, which causes high operating cost [1]. Therefore, research and development on the manufacturing process of LFT has been undertaken to eliminate semi-finished products [1].

The direct long-fiber reinforced thermoplastics (D-LFT) process, depicted in Figure 2.1, is an efficient manufacturing process starting from raw materials and leading to a final product [4], [5]. This process prevents the use of semi-finished products as well as reductions in fiber length during processing [2], [3]. The first step of D-LFT process is to dry polymer pellets. The dried pellets are then melted in the first twin-screw extruder. Through a waterfall film die, the melted polymer is temporally exposed to atmosphere while being transferred to the second twin-screw extruder, where continuous fiber rovings are fed directly into the polymer melt, thus maintaining long fiber lengths. At the end of the second twin-screw extruder, molten composite (plastificate) is ejected onto a conveyer

and cut to an appropriate size by a shear cutter. In the last step of the D-LTF process, the cut plastificates are transferred into a compression molding machine (press) to shape and solidify the final product.

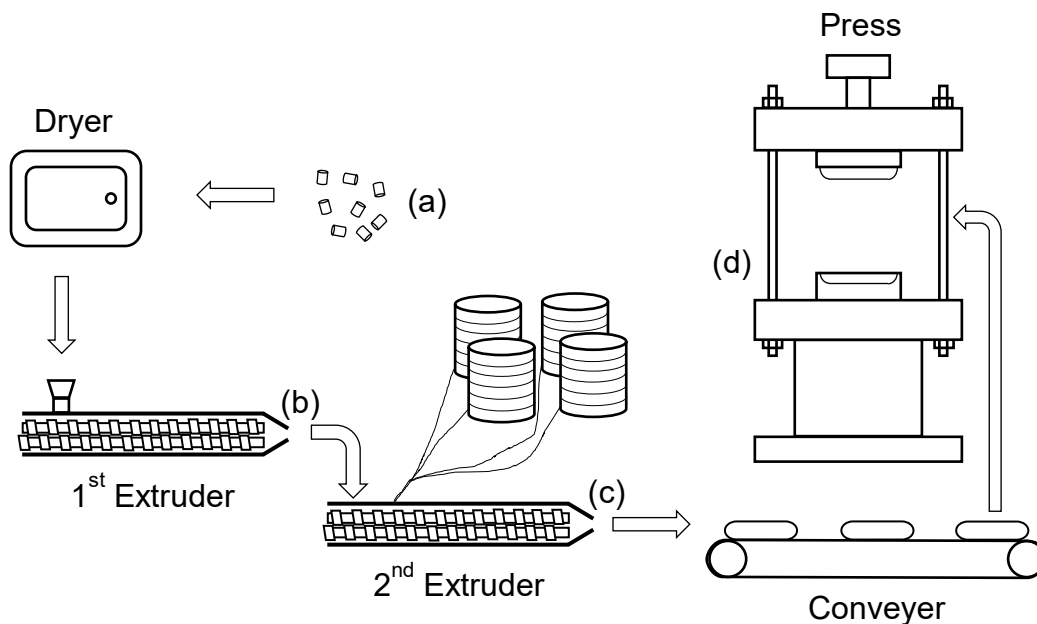


Figure 2.1 Schematic of D-LFT process with identified equipment as well as indicated locations for sample collection: (a) virgin, (b) first extruder, (c) second extruder, and (d) compressed plaque samples.

The two twin-screw extruders in series play an important role in the D-LFT process, especially the second twin-screw extruder which is designed for mixing continuous fibers with polymer melt. Judging from the past studies for fiber reinforced thermoplastics with different screw configurations in extruders [6], [7] and injection molding machines [8], it is expected that the screw configurations of the second twin-screw extruder in the D-LFT process can affect the quality of a D-LFT product.

There are three basic extruder screw elements: conveying elements, kneading elements, and mixing elements [9], [10]. A conveying element is used to transport material

and increase barrel pressure. The barrel pressure and the fill level of the material can be increased by decreasing the pitch (distance between two adjacent crests) of a screw. A kneading element is designed for both dispersive mixing and distributive mixing. A kneading element comprises kneading discs: a wide kneading disc provides dispersive mixing, while a narrow kneading disc leads to distributive mixing. A mixing element is a modified conveying element. Periodically placed channels allow materials to flow backward, which results in the melt stream splitting and recombination and thus encourages distributive mixing. When fibers are incorporated into polymer melt, the inclusion of mixing elements would be an appropriate choice because it can maximize distribution of fibers and minimize fiber breakage. However, when the mixing elements are used, shear stress and temperature may increase, which potentially causes degradation of polymer melt.

Polyamide 6 (PA6) is one of the most widely used engineering thermoplastics, and has excellent properties, such as high toughness, good impact and abrasion resistance, lubricity, and resistance to organic solvents [11], [12]. However, PA6 is susceptible to degradation [11], [13]-[17]. When PA6 is used as polymer matrix in the D-LFT process, it has the potential to undergo thermal [11], [18], mechanical [19], and thermo-oxidative [11], [20], [21] degradation. Therefore, it is important to investigate how screw configurations affect the degradation of PA6 throughout the D-LFT process. In this study, glass fiber-reinforced PA6 composites were produced through the D-LFT process by using different screw configurations in the second twin-screw extruder. The molecular weight, thermal decomposition, and crystallization behavior of the materials were characterized as a function of locations in the D-LFT process line.

## 2.1 Experimental

### 2.1.1 Materials and fabrication of composites

In this study, PA6 (Ultramid® 8202 HS), supplied by BASF in pellet form, was used as the matrix, and glass fiber (StarRov® 886 RXN), supplied by Johns Manville and provided in roving form, was used as the reinforcement. The composites were manufactured at the Fraunhofer Project Centre for Composites Research at the University of Western Ontario. PA6 was combined with 30 wt% of the glass fibers using an industrial-scale Dieffenbacher D-LFT line. The D-LFT line consisted of a series of a dryer, two extruders, a conveyer and a 2,500-ton hydraulic press (DCP-U 2500/2200, Dieffenbacher). The dryer (LUXOR S 120, Motan Colotronic) was set at 80°C and dried the PA6 pellets for 16 hours. The first extruder was a compounding twin-screw extruder (ZSE-60HP-28D, Leistritz) with a 60 mm diameter and a length to diameter ratio (L/D) of 28; the second extruder was a mixing twin-screw extruder (ZSG-75 P-17D, Leistritz) with a 75 mm diameter and a L/D of 17. The temperature set point for both extruders was 280 °C, and the screw speeds of the first and second extruders were 161 rpm and 50 rpm, respectively. The flow rate of material from the second extruder was 204.8 kg/h.

Figure 2.2 shows the two screw configurations used in this study for the second extruder: one had conveying elements only (named the conveying screw) (Fig. 2.2a) and the other included mixing elements as well as conveying elements (named the mixing screw) (Fig. 2.2b). It was expected that the mixing screw would generate higher shear stress in the composite melt than the conveying screw. The labeling method for the screw elements is as follows: GFA and GFM represent a conveying element and a mixing element, respectively. The first digit indicates the number of flights, the second digit

specifies the pitch (in mm), and the last digit states the length of the element (in mm). The material flow direction is from left to right in the figure.

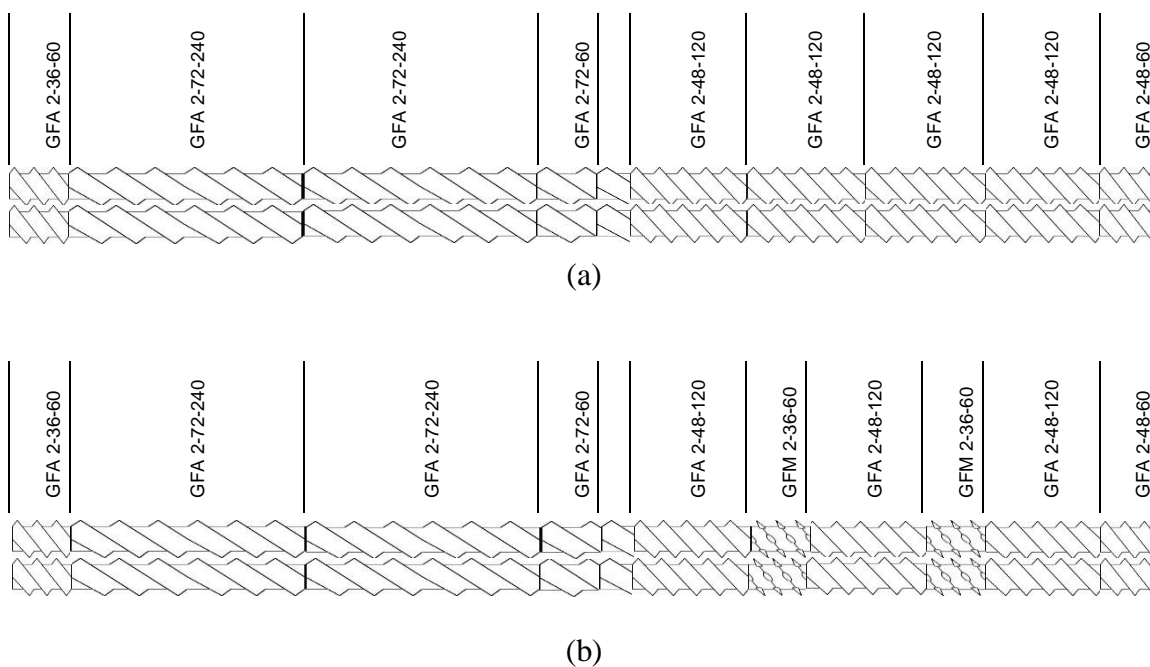


Figure 2.2 Screw configurations of second extruder: (a) conveying screw and (b) mixing screw, where flow direction of material is from left to right.

The conveyor belt temperature was set to 260°C. For the hydraulic press, the mold temperature was set to 120°C, and the force applied to the plastificate was set to 5,000 kN for 30 s. Samples were collected from four locations along the D-LFT process line: (a) as received (i.e., virgin PA6), (b) directly after the first extruder (taken from the waterfall film die), (c) directly after the second extruder, and (d) a compressed plaque.

### 2.1.2 Triple detection gel permeation chromatography (GPC)

Absolute molecular weight distribution and intrinsic viscosity of the polymer matrix (i.e., PA6) were measured by gel permeation chromatography (GPC) coupled with triple

detectors: a refractive index (RI) detector, a light scattering detector, and a four-capillary differential viscometer (Viscotek TDA302 and GPCmax, Malvern Panalytical). Potassium trifluoroacetate (KTFA) at 0.05 M concentration in 1,1,1,3,3,3-hexafluoro-2-propanol (HFIP) was employed as the mobile phase, and the flow rate was 0.7 mL/min. Samples were dissolved in the 0.05 M KTFA/HFIP solution and then filtered through a 0.22  $\mu\text{m}$  polytetrafluoroethylene (PTFE) syringe filter to remove any undissolved material. A 50  $\mu\text{L}$  sample was eluted through two columns held at 35°C. Poly(methyl methacrylate) (PMMA) standards were used for calibration.

The polydispersity index (*PDI*) of the polymer matrix (i.e., PA6) was calculated by

$$PDI = \frac{M_w}{M_n} \quad (1)$$

where  $M_w$  and  $M_n$  are, respectively, the weight-average molecular weight and the number-average molecular weight.

The intrinsic viscosity can be correlated with molecular weight using the following Mark-Houwink equation [22], [23]:

$$[\eta] = KM^\alpha \quad (2)$$

where  $K$  and  $\alpha$  are constants, and  $M$  is molecular weight.

The  $\alpha$  value indicates configuration that a polymer adopts in solution, and is a function of polymer architecture, solvent used, and temperature [22]-[25]. When branching occurs in the polymer, the  $\alpha$  value decreases provided that the same solvent is used and the

temperature is fixed [23]. Therefore, the  $\alpha$  value was measured to examine if branching occurs through the D-LFT process. Eq. 2 can be transformed into the logarithmic form,

$$\log[\eta] = \log K + \alpha \log M \quad (3)$$

So that the  $\alpha$  value (slope) could be determined by plotting  $\log[\eta]$  against  $\log M$ .

### 2.1.3 Thermogravimetric analysis

The thermal stability of both polymer and composite samples was investigated using a thermogravimetric analyzer (TGA) (TGA Q50, TA Instruments). The mass of the samples was 8.5 mg ( $\pm 0.5$  mg). The temperature profile of the TGA analysis conducted was heating ramp of 10 °C/min from room temperature to 500 °C. The purge gas was nitrogen and flow rates were set to 40 mL/min and 60 mL/min to the balance and sample areas, respectively.

The degree of conversion (or decomposition),  $\alpha$ , of the sample was calculated by using:

$$\alpha = \left( \frac{M_o - M_t}{M_o - M_f} \right) \times 100 \quad (4)$$

where  $M_o$ ,  $M_t$ ,  $M_f$  are, respectively, the mass at the beginning of the decomposition profile, the corresponding mass at the decomposition level being calculated (e.g. mass when 20% decomposed), and the final mass after decomposition.

The activation energy for decomposition  $E_a$  was calculated from the TGA curves by the Horowitz-Metzger method [26]:

$$\ln[\ln(1 - \alpha)^{-1}] = \frac{E_a \theta}{R(T_{max})^2} \quad (5)$$

where  $\alpha$  is the degree of conversion (or decomposition),  $\theta$  is  $(T - T_{max})$  [K],  $T$  is the temperature [K],  $T_{max}$  is the temperature where the maximum rate of mass loss occurs [K], and  $R$  is the gas constant [8.31 J/(mol K)]. The activation energy for decomposition (slope) was determined by plotting  $\ln[\ln(1 - \alpha)^{-1}]$  versus  $\theta$ .

#### 2.1.4 Differential scanning calorimetry

Non-isothermal and isothermal crystallization behaviors of the materials were studied using a differential scanning calorimeter (DSC) (Q2000, TA Instruments). A nitrogen purge gas with a flow rate of 50 mL/min was used. The mass of the samples was 8.5 mg ( $\pm 0.5$  mg) in both non-isothermal and isothermal measurements. In the non-isothermal crystallization measurements, a sample was first heated to 270 °C at 10 °C/min and held at that temperature for 5 minutes to erase the thermal history in the collected sample. The sample was then cooled to 20 °C at 10 °C/min and held at that temperature for 5 minutes. Lastly, the sample was reheated to 270 °C at 10 °C/min. The degree of crystallinity  $X_c$  of the sample was calculated from the second DSC heating curve and the following equation:

$$X_c = \frac{\Delta H_m}{\Delta H_f(1 - W_f)} \times 100\% \quad (6)$$

where  $\Delta H_m$  is enthalpy of fusion;  $\Delta H_f$  is enthalpy of fusion of fully crystalline PA6, which is taken to be 230 J/g [27]; and  $W_f$  is the weight fraction of fiber.



In the isothermal crystallization measurements, a sample was first heated to 270 °C at 10 °C/min and held at that temperature for 5 minutes to erase the thermal history of the collected sample. Then, the sample was cooled to the isothermal temperature of 200 °C at 50 °C/min and held at that temperature for 30 minutes to allow the sample to fully crystallize. Using the isothermal DSC curves, relative degree of crystallinity  $X_{rel}$  was calculated as follows:

$$X_{rel} = \frac{\int_0^t \frac{dH(t)}{dt} dt}{\int_0^\infty \frac{dH(t)}{dt} dt} \quad (7)$$

where the isothermal DSC curve is integrated between  $t = 0$  and  $t$ , and divided by the overall crystallization area.

The crystallization kinetics were analyzed using the Avrami equation. According to the Avrami model [28], [29], the relative degree of crystallinity  $X_{rel}$  is described as follows:

$$X_{rel}(t) = 1 - \exp(-kt^n) \quad (8)$$

where  $n$  is the Avrami exponent that depends on the nucleation mechanism and growth geometry of crystals,  $k$  is the crystallization rate constant that involves both nucleation and growth rate parameters, and  $t$  is time.

The parameters  $n$  (slope) and  $k$  (intercept) were determined by plotting  $\log[-\ln(1 - X_{rel}(t))]$  against  $\log t$ . The crystallization half time  $t_{1/2}$ , which is defined as the time from crystallization onset until 50% completion, was calculated as follows:

$$t_{1/2} = \left(\frac{\ln 2}{k}\right)^{\frac{1}{n}} \quad (9)$$

## 2.2 Results and Discussion

### 2.2.1 Discoloration

Figure 2.3 shows the color changes that took place in the material throughout the D-LTF process using the different screw configurations in the second extruder. A slight color change was found after drying. This color change was possibly due to air exposure (thermo-oxidative degradation) in the convection oven while the moisture was removed from the PA6. The sample became light yellow after the first extruder and then dark yellow after the second extruder. This was possibly due to the high temperature (thermal degradation) and shear stress (mechanical degradation) in the extruders. The sample became brown after the conveyer and press possibly due to air exposure on the conveyer (thermo-oxidative degradation).




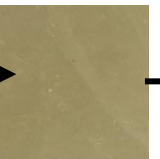






Screw Configuration	Process Location				
	Virgin	Dry	1 <sup>st</sup> Extruder	2 <sup>nd</sup> Extruder	Compressed Plaque
Conveying Screw					
Mixing Screw					

Figure 2.3 Material discoloration throughout D-LTF process with different screw configurations.

When samples processed with different screw configurations are compared, the samples taken after the second extruder showed similar discoloration. However, the compressed plaque samples processed with the mixing screw had a higher degree of discoloration (i.e., darker) than those with the conveying screw.

### 2.2.2 Molecular weight and intrinsic viscosity

Figure 2.4 shows weight-average molecular weight (Fig. 2.4a) and *PDI* (Fig. 2.4b) of the PA6 matrix processed under different process locations and screw configurations. The molecular weight slightly decreased with process progression up to the second extruder samples, but increased from the second extruder samples to the compressed plaque samples. On the other hand, the *PDI* increased slightly with process progression up to the second extruder samples, and increased much further from the second extruder samples to the compressed plaque samples. When samples processed using the two different screws are compared, the samples produced using the mixing screw had lower molecular weight and *PDI* than those produced using the conveying screw.

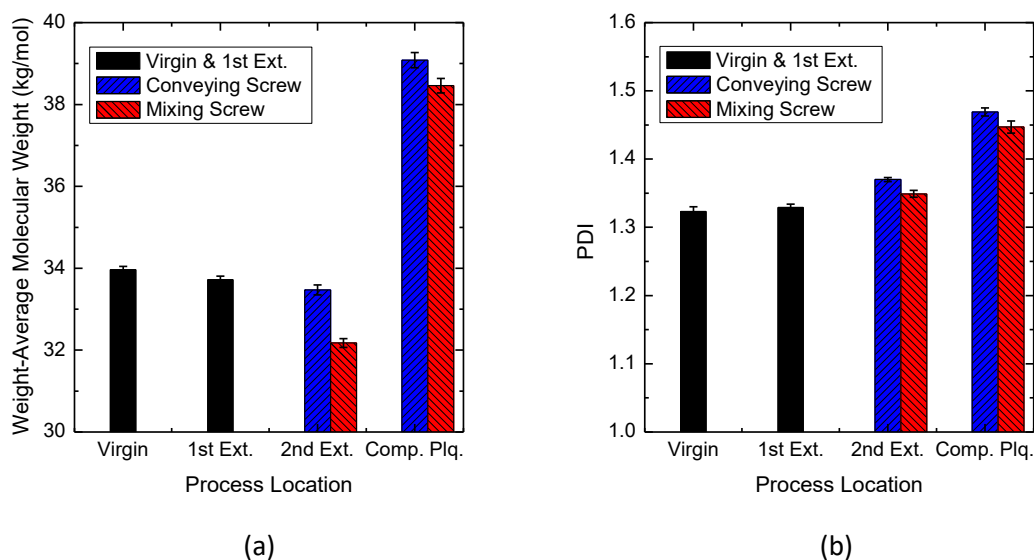


Figure 2.4 (a) Weight-average molecular weight and (b) *PDI* of virgin, first extruder, second extruder, and compressed plaque samples processed with different screw configurations.

Figure 2.5a shows Mark-Houwink plots, that is, plots of  $\log[\eta]$  versus  $\log M$ , of samples processed under different process locations and screw configurations. There were two distinct groups of lines. One group includes samples in the earlier stages of the D-LFT process (i.e., the virgin, first extruder, and second extruder samples), and the other group has samples from the last stage of the D-LFT process (i.e., the compressed plaque samples). Figure 2.5b shows the slopes from the Mark-Houwink plots (i.e.,  $\alpha$  values). The  $\alpha$  value decreased slightly with process progression up to the second extruder samples. However, the  $\alpha$  value decreased significantly from the second extruder samples to the compressed plaque samples, which indicates that much more branching of the PA6 molecules occurred from the second extruder samples to the compressed plaque samples. When samples processed using two different screws are compared, the screw configurations had little effect on the  $\alpha$  value.

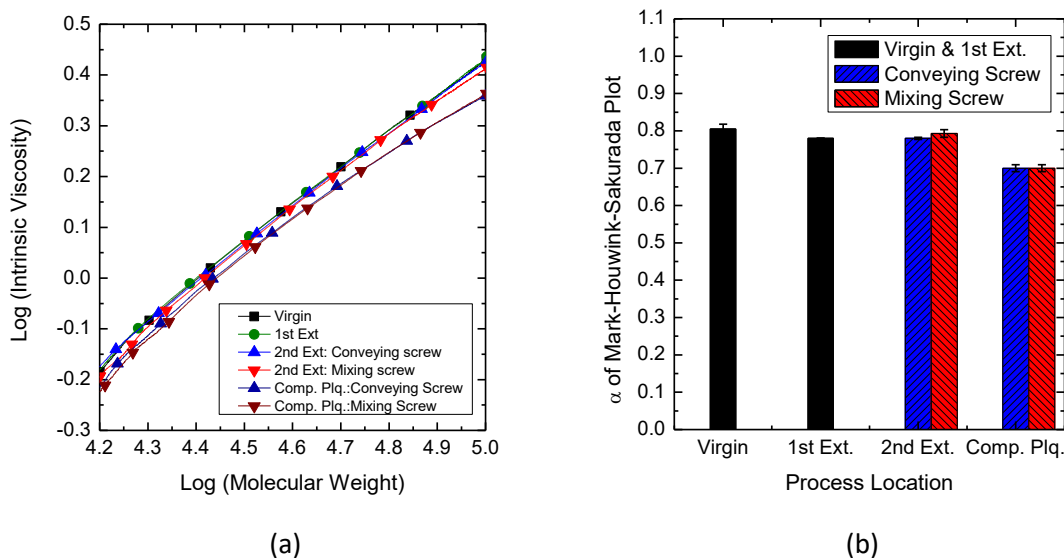


Figure 2.5 (a) Mark-Houwink plots and (b)  $\alpha$  values obtained from Mark-Houwink plots of virgin, first extruder, second extruder, and compressed plaque samples processed with different screw configurations.

The results obtained from Figs. 2.4 and 2.5 suggest that chain scission of the PA6 polymer chains was the dominant mechanism with process progression up to the second extruder samples. This is mainly caused by thermal and mechanical degradation of the PA6 matrix. On the other hand, branching of PA6 molecules was the prevailing mechanisms from the second extruder samples to the compressed plaque samples, which is mainly caused by thermo-oxidative degradation of the PA6 matrix. Various chemical reaction mechanisms for chain scission and branching of PA6 molecules were reported previously [11], [30]-[35]. Chain scission may occur through cleavage of a C-N bond [11], [30], [32], [35]; cleavage of a CH<sub>2</sub>-CH<sub>2</sub> linkage [11], [34]; and/or hydrolysis of an amide C(O)-NH [11], [30], [32], [34]. Meanwhile, branching may occur through condensation reaction between a carbonyl group (formed by oxidation [11], [30], [31], [33] and/or condensation reaction of the carboxyl chain-ends [11], [30], [32], [34]) and an amine chain-

end [11], [30]–[32]; and/or condensation reaction between a secondary amine group (formed by condensation reaction of amine chain-ends [11], [30], [32], [34]) and a carboxyl chain-end [11]. Further research into the chemical reaction mechanisms that occurred during the D-LFT process is required.

### 2.2.3 Thermal decomposition

Figure 2.6 shows typical thermogravimetric profiles obtained from samples processed using different screw configurations and taken from different process locations. The figure indicates that all the samples had a single-stage decomposition of the PA6 matrix. Figure 2.7 shows typical Horowitz-Metzger plots, that is, plots of  $\ln[\ln(1 - \alpha)^{-1}]$  versus  $\theta$ . The figure indicates that the trend lines for all the samples were almost linear, and the slope decreased with process progression up to the second extruder samples. The slopes of trend lines were used to calculate activation energy.

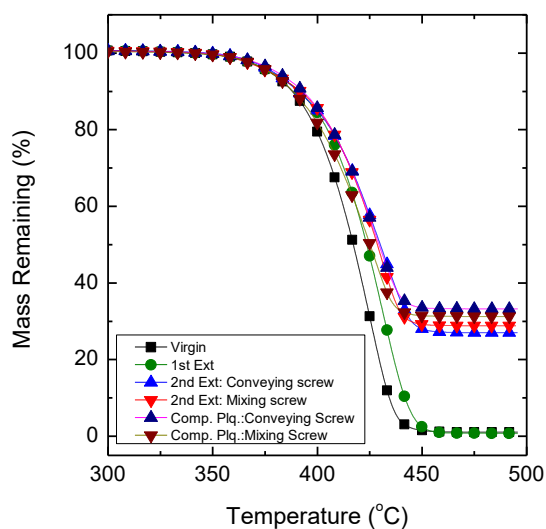


Figure 2.6 TGA curves of virgin, first extruder, second extruder, and compressed plaque samples processed with different screw configurations.

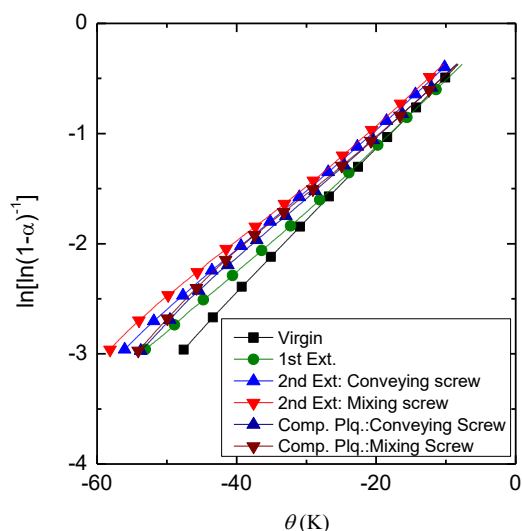


Figure 2.7 Horowitz-Metzger plots of virgin, first extruder, second extruder, and compressed plaque samples processed with different screw configurations.

Figure 2.8 shows the activation energy of samples processed using different screw configurations and taken from different process locations. The activation energy decreased with process progression from the virgin samples to the second extruder samples, which may be attributed to the decrease of the molecular weight of the PA6 matrix (see Fig. 2.4). However, the activation energy was nearly unchanged (or only slightly increased) in the later process stages from the second extruder samples to the compressed plaque samples. It should be noted that the molecular weight of the PA6 matrix increased in the later process stages, and the compressed plaque samples had the highest molecular weight observed during the D-LFT process (see Fig. 2.4). The increase in molecular weight from the second extruder samples to the compressed plaque samples was caused by branching during the thermo-oxidative degradation process occurring as the material traveled the conveyor, and such molecules may be less thermally stable (i.e., lower activation energy) than the original, linear structure of the PA6 matrix. It should also be noted that, as shown in Fig.

2.3, significant discoloration occurred in the compressed plaque samples. It is known that the formation of char can increase the activation energy [20], [36]. Therefore, one may speculate that the negative effect of the molecular changes of the PA6 matrix and the positive effect of the char formation led to the approximately constant activation energy from the second extruder samples to the compressed plaque samples. Further research into the mechanisms leading to the changes in the activation energy is required.

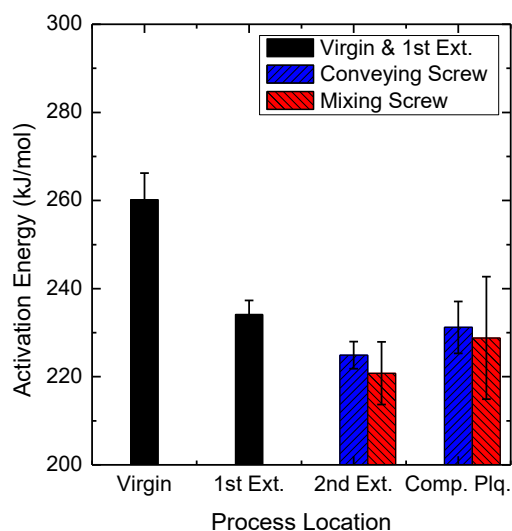


Figure 2.8 Activation energy of virgin, first extruder, second extruder, and compressed plaque samples processed with different screw configurations.

## 2.2.4 Crystallization

### 2.2.4.1 Non-Isothermal Crystallization

Figure 2.9 shows typical non-isothermal DSC cooling curves (Fig. 2.9a) and subsequent heating curves (Fig. 2.9b) of samples processed using different screw configurations and collected from different process locations. Table 2.1 summarizes the thermal properties that were obtained from the DSC cooling and heating curves, including the crystallization



peak temperature ( $T_c$ ), the enthalpy of crystallization ( $\Delta H_c$ ), the melting peak temperatures ( $T_{m1}$ ,  $T_{m2}$ ), the enthalpy of fusion ( $\Delta H_m$ ) and the degree of crystallinity ( $X_c$ ). The table suggests that the crystallization peak temperature, obtained from the DSC cooling curves, increased throughout the process up to the second extruder, that is, the virgin samples < the first extruder samples < the second extruder samples and the compressed plaque samples. On the other hand, the screw configurations had little effect on the crystallization peak temperature of both the second extruder samples and compressed plaque samples.

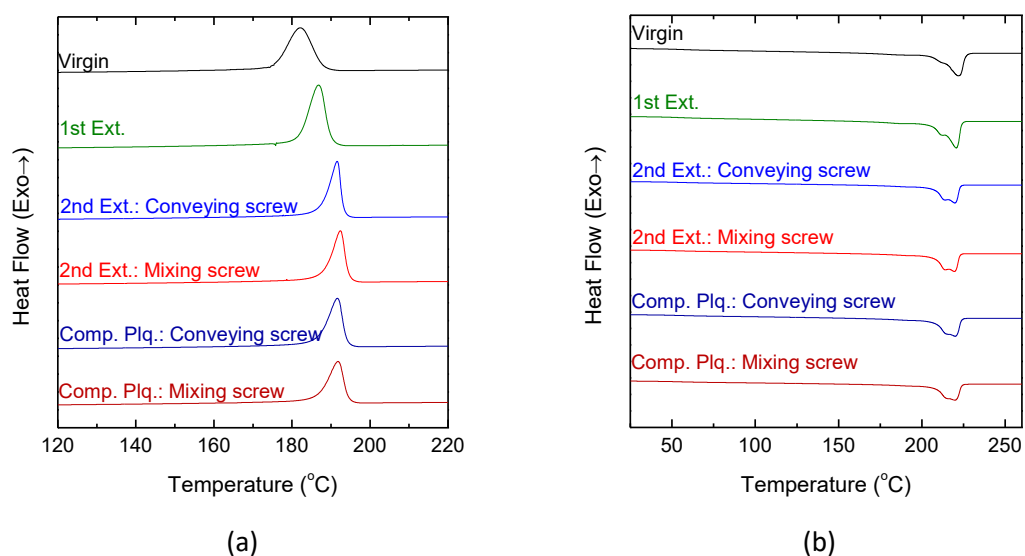


Figure 2.9 Non-isothermal DSC curves of virgin, first extruder, second extruder, and compressed plaque samples processed with different screw configurations: (a) cooling curves and (b) heating curves.

Table 2.1 Non-isothermal crystallization data of materials collected within D-LFT process. The numbers in the parenthesis are the standard deviations ( $n = 3$ ).

Process Location	Screw Configuration	$T_c$ (°C)	$\Delta H_c$ (J/g)	$T_{m1}$ (°C)	$T_{m2}$ (°C)	$\Delta H_m$ (J/g)	$X_c$ (%)
<b>Virgin</b>		182.2 (0.5)	66.3 (2.9)	212.3 (0.9)	221.9 (0.6)	67.0 (1.8)	29.1 (0.8)
	<b>First Extruder</b>	187.0 (0.2)	68.3 (0.8)	212.4 (0.3)	220.4 (0.2)	79.4 (2.2)	34.5 (0.9)
<b>Second Extruder</b>	Conveying Screw	191.3 (0.4)	49.6 (1.0)	214.5 (1.2)	219.9 (0.5)	56.7 (1.8)	35.2 (1.1)
	Mixing Screw	192.4 (0.1)	49.2 (1.3)	214.0 (0.0)	219.4 (0.1)	56.9 (0.6)	35.3 (0.3)
<b>Compressed Plaque</b>	Conveying Screw	191.6 (0.0)	50.2 (1.9)	215.6 (0.2)	220.0 (0.1)	60.2 (2.1)	37.4 (1.3)
	Mixing Screw	191.3 (0.8)	44.4 (1.9)	215.7 (0.1)	220.5 (1.0)	53.7 (2.0)	33.3 (1.2)

Two melting peaks ( $T_{m1}$  and  $T_{m2}$ , where  $T_{m1} < T_{m2}$ ) were observed on the DSC heating curves (Fig. 2.9b). These are associated with a difference in melting temperatures between the two phases present in the morphology ( $\alpha$  and  $\gamma$ ) of PA6 crystallites. The  $\alpha$  phase has polymer chains fully extended and oriented in an anti-parallel fashion while the  $\gamma$ -phase has polymer chains twisted at an angle of approximately  $60^\circ$  to maintain complete satisfaction of hydrogen bonds [37]–[40]. In general, the  $\gamma$ -phase is formed more favorably than the  $\alpha$ -phase under process conditions of high cooling rate, low isothermal crystallization temperature, and high shear stress [39]. Fig. 2.9b shows that the first melting peak gradually became more pronounced with process progression, which could be a result of the amount of  $\gamma$ -phase increasing [38]. Although it was expected that the mixing screw would generate higher shear stress in the composite melt than the conveying screw, the results suggest that the screw configurations had little effect on the two melting peaks or the degree of crystallinity.

#### 2.2.4.2 Isothermal Crystallization

Figure 2.10 shows typical isothermal DSC curves (isothermal temperature of 200 °C) of samples processed using different screw configurations and collected from different process locations. The figure suggests that crystallization speed increased with process progression up to the second extruder samples and was unchanged from the second extruder samples to the compressed plaque samples. Figure 2.11 shows typical Avrami plots, that is, plots of  $\log[-\ln(1 - X_{rel}(t))]$  versus  $\log t$ . There were two distinct groups of lines. One group includes samples in the earlier stages of the D-LFT process (i.e., the virgin and first extruder samples), and the other group has samples at the later stage of the D-LFT process (i.e., the second and compressed plaque samples). The lines moved to the left as the process progressed. The kinetic parameters determined from the Avrami equation are summarized in Table 2.2. The Avrami constant,  $n$ , decreased after the second extruder samples, which suggests that the addition of glass fiber had an influence on the crystal nucleation mechanisms in PA6.

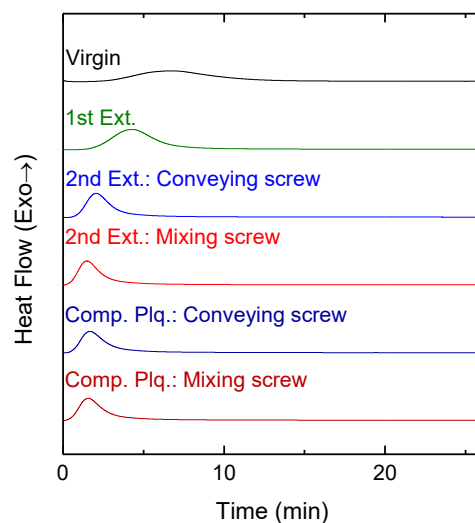


Figure 2.10 Isothermal DSC curves of virgin, first extruder, second extruder, and compressed plaque samples processed with different screw configurations.

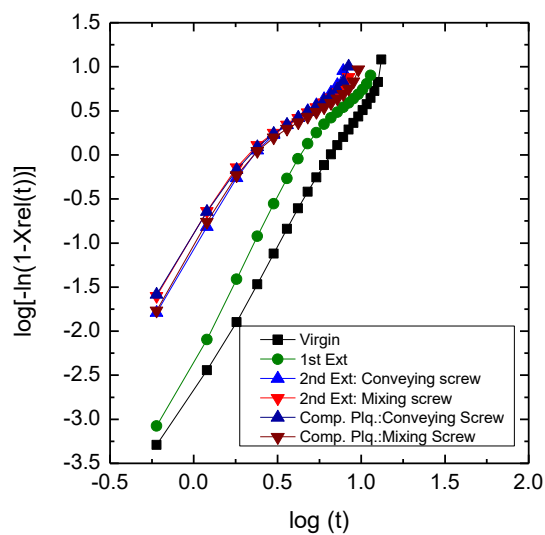


Figure 2.11 Avrami plots of virgin, first extruder, second extruder, and compressed plaque samples processed with different screw configurations.

Table 2.2 Avrami parameters of materials collected within D-LFT process. The numbers in the parenthesis are the standard deviations ( $n = 3$ ).

<b>Process Location</b>	<b>Screw Configuration</b>	<b><math>n</math></b>	<b><math>k</math> (<math>\text{min}^{-n}</math>)</b>
<b>Virgin</b>		2.89 (0.06)	$3.31 \times 10^{-3}$ ( $0.53 \times 10^{-3}$ )
<b>First Extruder</b>		3.03 (0.14)	$7.23 \times 10^{-3}$ ( $0.71 \times 10^{-3}$ )
<b>Second Extruder</b>	Conveying Screw	2.26 (0.05)	$9.02 \times 10^{-2}$ ( $1.58 \times 10^{-2}$ )
	Mixing Screw	1.90 (0.08)	$1.52 \times 10^{-1}$ ( $0.05 \times 10^{-1}$ )
<b>Compressed Plaque</b>	Conveying Screw	1.91 (0.13)	$1.48 \times 10^{-1}$ ( $0.13 \times 10^{-1}$ )
	Mixing Screw	1.95 (0.07)	$1.19 \times 10^{-1}$ ( $0.07 \times 10^{-1}$ )

Figure 2.12 shows the crystallization half-time from samples processed under different screw configurations and process locations. The crystallization half-time decreased in the earlier stages of the process, that is, the virgin samples > the first extruder samples > the second extruder samples. The decrease of crystallization half-time in the first extruder samples may have been caused by (i) decreased molecular weight, (ii) impurities incorporated during extrusion creating nucleation sites, and/or (iii) memory effects imposed upon the polymer during extrusion and remaining during thermal analysis [39]. The further decrease of crystallization half-time in the second extruder samples was possibly a result of the three factors mentioned above and/or the incorporation of glass fibers in the second extruder. Fibers, when introduced to a polymer, can act as heterogeneous nucleating agents (NA) during crystallization [41]–[43]. If the fibers did act in such a way, they may have provided nucleation sites for crystal growth and decreased the crystallization half-time.

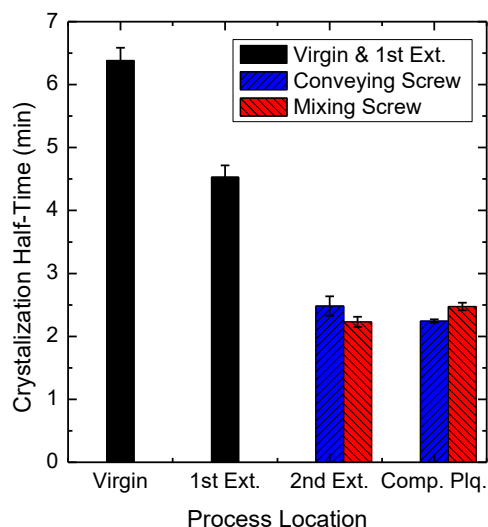


Figure 2.12 Crystallization half-time of virgin, first extruder, second extruder, and compressed plaque samples processed with different screw configurations.

The crystallization half-time was unchanged in the later stages of the process, that is, between the second extruder samples and the compressed plaque samples. In addition, the screw configurations had little influence on the crystallization half-time for either the second extruder samples or compressed plaque samples. However, as mentioned above, the triple detection GPC results showed an increase of molecular weight and branching of the PA6 matrix between the second extruder samples and the compressed plaque samples (see Figs. 2.4 and 2.5), which may have led to increase of crystallization half-time due to interference with chain folding. It is speculated that the fiber incorporation may have had a much greater influence on the crystallization half-time than the molecular changes of the PA6 matrix.

## 2.3 Conclusions

Effects of the screw configurations on the thermal properties of glass fiber reinforced PA6 were studied at the four locations within the D-LFT process. Triple Detection GPC results showed that molecular weight slightly decreased with process progression up to the second extruder samples by chain scission of PA6 molecules, but increased in the later stages of the D-LFT process (i.e., from the second extruder samples to the compressed plaque samples) by branching of PA6 molecules. In addition, the samples produced using the mixing screw had lower molecular weight of the PA6 matrix than those produced using the conveying screw. However, TGA results showed that the screw configurations had little effect on the activation energy for decomposition. DSC crystallization analysis also revealed no substantial changes to the degree of crystallinity and crystallization half-time with the change of the screw configurations. These results suggest that the difference in molecular weight of the PA6 matrix caused by the screw configurations had little influence on the thermal stability and crystallization behavior of the composites.

## References

- [1] U. K. Vaidya and K. K. Chawla, "Processing of fibre reinforced thermoplastic composites," *Int. Mater. Rev.*, vol. 53, no. 4, pp. 185–218, Jul. 2008.
- [2] M. Schemme, "LFT – development status and perspectives," *Reinf. Plast.*, vol. 52, no. 1, pp. 32–39, Jan. 2008.
- [3] P. E. W. Krause, F. Henning, S. Troster, O. Geiger, "LFT-D – A Process Technology for Large Scale Production of Fiber Reinforced Thermoplastic Components," *J. Thermoplast. Compos. Mater.*, vol. 16, no. July 2003, pp. 289–302, 2003.
- [4] T. Whitfield, T. Kuboki, J. Wood, V. Ugresic, S. Sathyanarayana, and K. Dagnon, "Thermal properties of glass fiber reinforced polyamide 6 composites throughout the direct long-fiber reinforced thermoplastic process," *Polym. Eng. Sci.*, vol. 58, no. 1, pp. 46–54, Jan. 2018.
- [5] T. Whitfield, T. Kuboki, J. Wood, V. Ugresic, S. Sathyanarayana, and K. Dagnon, "Effects of process parameters on thermal properties of glass fiber reinforced polyamide 6 composites throughout the direct long-fiber-reinforced thermoplastics process," *Polym. Eng. Sci.*, vol. 58, no. S1, pp. E114–E123, May 2018.
- [6] S. H. Bumm, J. L. Whitey, and A. I. Isayev, "Glass Fiber Breakup in Corotating Twin Screw Extruder: Simulation and Experiment," *Polym. Compos.*, 2012.
- [7] P. Ren and G. Dai, "Fiber dispersion and breakage in deep screw channel during processing of long fiber-reinforced polypropylene," *Fibers Polym.*, vol. 15, no. 7, pp. 1507–1516, 2014.



- [8] A. Inoue, K. Morita, T. Tanaka, Y. Arao, and Y. Sawada, "Effect of screw design on fiber breakage and dispersion in injection-molded long glass-fiber-reinforced polypropylene," *J. Compos. Mater.*, vol. 49, no. 1, pp. 75–84, 2015.
- [9] K. Kohlgruber, *Co-Rotating Twin-Screw Extruders: Fundamentals, Technology, and Applications*. Munich, Germany: Carl Hanser Publishers, 2008.
- [10] C. I. Chung, *Extrusion of Polymers: Theory and Practice*, 2nd ed. Munich, Germany: Carl Hanser Publishers, 2011.
- [11] S. V. Levchik, E. D. Weil, and M. Lewin, "Thermal decomposition of aliphatic nylons," *Polym. Int.*, vol. 48, no. 7, pp. 532–557, 1999.
- [12] F. Faridirad, S. Ahmadi, and M. Barmar, "Polyamide/Carbon Nanoparticles Nanocomposites: A Review," *Polym. Eng. Sci.*, vol. 57, no. 5, pp. 475–494, May 2017.
- [13] A. G. Pedroso, L. H. I. Mei, J. A. M. Agnelli, and D. S. Rosa, "The influence of the drying process time on the final properties of recycled glass fiber reinforced polyamide 6," *Polym. Test.*, vol. 21, no. 2, pp. 229–232, 2002.
- [14] R. D. Davis, J. W. Gilman, and D. L. VanderHart, "Processing degradation of polyamide 6/montmorillonite clay nanocomposites and clay organic modifier," *Polym. Degrad. Stab.*, vol. 79, no. 1, pp. 111–121, 2003.
- [15] M. I. Kohan, *Nylon Plastics Handbook*. New York, USA: Hanser Publishers, 1995.
- [16] K. Pielichowski and J. Njuguna, *Thermal Degradation of Polymeric Materials*.

Shawbury, UK: Rapra Technology Limited, 2005.

- [17] R. S. Lehrle, I. W. Parsons, and M. Rollinson, "Thermal degradation mechanisms of Nylon 6 deduced from kinetic studies by pyrolysis-g.c.," *Polym. Degrad. Stab.*, vol. 67, no. 1, pp. 21–33, 2000.
- [18] C. L. Beyler and M. M. Hirschler, "Thermal Decomposition of Polymers," in *SFPE Handbook of Fire Protection Engineering*, 4th ed., Quincy, USA: National Fire Protection Association, 2008, pp. 110–131.
- [19] J. E. Crespo, F. Parres, M. A. Peydró, and R. Navarro, "Study of rheological, thermal, and mechanical behavior of reprocessed polyamide 6," *Polym. Eng. Sci.*, vol. 53, no. 4, pp. 679–688, Apr. 2013.
- [20] X. Zuo, H. Shao, D. Zhang, Z. Hao, and J. Guo, "Effects of thermal-oxidative aging on the flammability and thermal-oxidative degradation kinetics of tris(tribromophenyl) cyanurate flame retardant PA6/LGF composites," *Polym. Degrad. Stab.*, vol. 98, no. 12, pp. 2774–2783, 2013.
- [21] L. Xia, B. Shentu, and Z. Weng, "Preparation of a novel stabilizer and its thermal-oxidative stabilization effect on polyamide 6," *Polym. Eng. Sci.*, vol. 54, no. 9, pp. 2197–2206, Sep. 2014.
- [22] P. C. Hiemenz and T. Lodge, *Polymer chemistry*, 2nd ed. Boca Raton, FL, USA: Taylor & Francis, 2007.
- [23] A. M. Striegel, W. W. Yau, J. J. Kirkland, and D. D. Bly, *Modern Size-Exclusion*

Liquid Chromatography, 2nd ed. Hoboken, NJ, USA: John Wiley & Sons, Inc., 2009.

- [24] J. M. Evans, "Gel permeation chromatography: A guide to data interpretation," *Polym. Eng. Sci.*, vol. 13, no. 6, pp. 401–408, Sep. 1973.
- [25] J. Brandrup, E. H. Immergut, and E. A. Grulke, Eds., *Polymer handbook*, 4th ed. New York, USA: John Wiley & Sons, Inc., 1999.
- [26] H. H. Horowitz and G. Metzger, "A New Analysis of Thermogravimetric Traces," *Anal. Chem.*, vol. 35, no. 10, pp. 1464–1468, 1963.
- [27] B. Wunderlich, "Crystal Melting," in *Macromolecular Physics*, New York, USA: Academic Press, 1973.
- [28] M. Avrami, "Kinetics of Phase Change. II Transformation-Time Relations for Random Distribution of Nuclei," *J. Chem. Phys.*, vol. 8, no. 212, pp. 212–224, 1940.
- [29] M. Avrami, "Granulation, Phase Change, and Microstructure Kinetics of Phase Change. III," *J. Chem. Phys.*, vol. 9, no. 2, pp. 177–184, 1941.
- [30] A. L. Bhuiyan, "Some aspects of the thermal stability action of the structure in aliphatic polyamides and polyacrylamides," *Polymer (Guildf.)*, vol. 25, no. 12, pp. 1699–1710, 1984.
- [31] T. Karstens and V. Rossbach, "Thermo - oxidative degradation of polyamide 6 and 6,6. Kinetics of the formation and inhibition of UV/VIS - active chromophores," *Die Makromol. Chemie*, vol. 190, no. 12, pp. 3033 – 3053, Jun. 1989.

- [32] S. V Levchik, L. Costa, and G. Camino, "Effect of the fire-retardant, ammonium polyphosphate, on the thermal decomposition of aliphatic polyamides: Part II—polyamide 6," *Polym. Degrad. Stab.*, vol. 36, no. 3, pp. 229–237, 1992.
- [33] P. Marechal, R. Legras, and J. M. Dekoninck, "Postcondensation and oxidation processes in molten polyamide 6," *J. Polym. Sci. Part A Polym. Chem.*, vol. 31, no. 8, pp. 2057–2067, Jun. 1993.
- [34] P. R. Hornsby, J. Wang, R. Rotheron, G. Jackson, G. Wilkinson, and K. Cossick, "Thermal decomposition behaviour of polyamide fire-retardant compositions containing magnesium hydroxide filler," *Polym. Degrad. Stab.*, vol. 51, no. 3, pp. 235–249, 1996.
- [35] S. V. Levchik, G. F. Levchik, A. I. Balabanovich, G. Camino, and L. Costa, "Mechanistic study of combustion performance and thermal decomposition behaviour of nylon 6 with added halogen-free fire retardants," *Polym. Degrad. Stab.*, vol. 54, no. 2–3, pp. 217–222, Nov. 1996.
- [36] K. Scully and R. Bissessur, "Decomposition kinetics of nylon-6/graphite and nylon-6/graphite oxide composites," *Thermochim. Acta*, vol. 490, no. 1–2, pp. 32–36, 2009.
- [37] N. Hiramatsu and S. Hirakawa, "Melting and Transformation Behavior of gamma form nylon6 under high pressure," *Polymer (Guildf.)*, vol. 14, no. 3, pp. 165–171, Mar. 1982.
- [38] S. M. Aharoni, "Crystallinity and Poymorphism in the n-Nylon Family," in n-

Nylons: Their Synthesis, Structure and Properties, Chichester, UK: John Wiley & Sons Ltd, 1997, pp. 34–70.

- [39] T. D. Fornes and D. R. Paul, “Crystallization behavior of nylon 6 nanocomposites,” *Polymer (Guildf.)*, vol. 44, no. 14, pp. 3945–3961, 2003.
- [40] S. Şanlı, A. Durmus, and N. Ercan, “Effect of nucleating agent on the nonisothermal crystallization kinetics of glass fiber- and mineral-filled polyamide-6 composites,” *J. Appl. Polym. Sci.*, vol. 125, no. S1, pp. E268–E281, 2012.
- [41] J. Liang, Y. Xu, Z. Wei, P. Song, G. Chen, and W. Zhang, “Mechanical properties, crystallization and melting behaviors of carbon fiber-reinforced PA6 composites,” *J. Therm. Anal. Calorim.*, vol. 115, no. 1, pp. 209–218, 2014.
- [42] U. Göschel, W. Lutz, and N. C. Davidson, “The influence of a polymeric nucleating additive on the crystallisation in glass fibre reinforced polyamide 6 composites,” *Compos. Sci. Technol.*, vol. 67, no. 11–12, pp. 2606–2615, 2007.
- [43] C. Guo, L. Zhou, and J. Lv, “Effects of expandable graphite and modified ammonium polyphosphate on the flame-retardant and mechanical properties of wood flour-polypropylene composites,” *Polym. Polym. Compos.*, vol. 21, no. 7, pp. 449–456, 2013.

## Chapter 3

### 3 Molecular Weight and Thermal Properties of Carbon Fiber Reinforced Polyamide 66 Composites throughout the Direct Long-Fiber Reinforced Thermoplastics Process

#### 3.1 Introduction

The direct long-fiber reinforced thermoplastics (D-LFT) process is an efficient manufacturing process starting from raw materials and leading to a final product. This process prevents the use of semi-finished products as well as reductions in fiber length during processing [1], [2], [3]. As depicted in Figure 3.1, the D-LFT process is a series of processes involving two twin-screw extruders, a conveyer, and a compression molding machine [4], [5]. The first step of D-LFT process is to dry polymer pellets. The dried pellets are melted in the first twin-screw extruder. The melted polymer is temporally exposed to atmosphere through a waterfall film die and transferred to the second twin-screw extruder, where continuous fiber rovings are fed directly into the polymer melt to maintain long fiber lengths. The molten composite (plastificate) ejected from the second twin-screw extruder is placed onto a conveyer, where it is cut to an appropriate size by a shear cutter. The cut plastificates are transferred into a compression molding machine (press) to shape and solidify the final product.

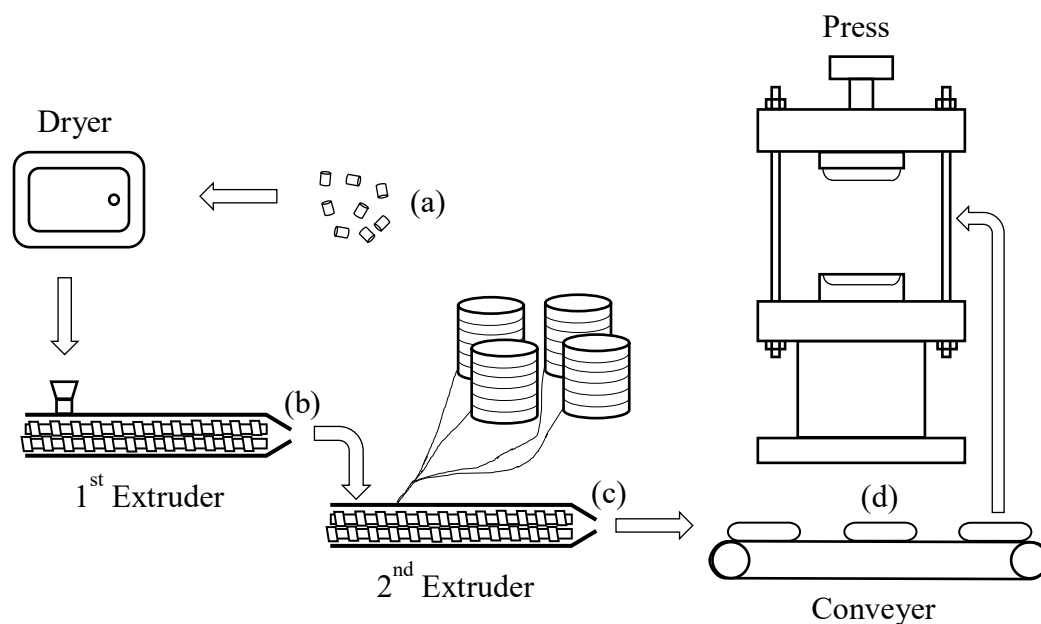


Figure 3.1 Schematic of the D-LFT process with identified equipment as well as indicated locations for sample collection: (a) virgin PA66, (b) first extruder, (c) second extruder, (d) half conveyer, and (e) compressed plaque samples.

Glass fibers have been widely used as reinforcements in the D-LFT process because they provide good performance at a lower cost [1], [2]. However, transportation industry, particularly automotive industry, seeks for D-LFT products with lighter weight and higher performance. Carbon fibers are candidates as reinforcements to reduce density and improve performance of D-LFT products. Carbon fibers have low density as well as excellent mechanical properties, thermal properties, electrical and thermal conductivities, and chemical resistance [6], [7]. Furthermore, recent decrease of carbon fiber prices facilitates their use in D-LFT products.

Polypropylene has been widely used as a polymer matrix in the D-LFT process because they provide good processability at a lower cost [1], [2]. However, it has relatively low mechanical properties and service temperatures. Polyamides (PA) are candidates as a

polymer matrix for carbon fibers to improve performance of D-LFT products. Polyamide (PA) has good mechanical properties, thermal properties, wear resistance, chemical resistance, and fire resistance [8], [9]. Polyamide 6 (PA6) and polyamide 66 (PA66) are the most commonly used PAs as engineering plastics [9]. PA66 has higher modulus [8], [10], [11] and absorbs less water [8] than PA6. Moreover, PA66 has a higher melting temperature [8], [10], [11], glass transition temperature [10], [11] and deflection temperature [8], [10] than PA6.

However, PA is susceptible to degradation [9], [12]-[17]. When PA is used as polymer matrix in the D-LFT process, it has the potential to undergo thermal [9], [13], [18], mechanical [19], and thermo-oxidative [9], [20], [21] degradation. In contrast, PA crosslinks when it is exposed to air under high temperature [9]. In particular, PA66 shows higher tendency to undergo crosslinking than other PAs [9]. As mentioned earlier, material passes through a unique process route in the D-LFT process. Therefore, when PA66 is used as the polymer matrix, it is imperative to understand how the process sequence affects PA66 molecules. In this study, carbon fiber-reinforced PA66 composites were produced through the D-LFT process. Molecular weight, thermal decomposition, and crystallization behavior of the materials were characterized as a function of location in the D-LFT process line.



## 3.2 Experimental

### 3.2.1 Materials and fabrication of composites

In this study, PA66 (Ultradid® A3W), supplied by BASF in pellets form was used as the matrix; and carbon fiber (Panex® 35-62), supplied by Zoltek and provided in roving form, was used as the reinforcement. Composites were manufactured at the Fraunhofer Project Centre for Composites Research at the University of Western Ontario. PA66 was combined with 40 wt% of the carbon fibers using an industry-scale Dieffenbacher D-LFT line. The D-LFT line was a series of a dryer, two extruders, a conveyer and a 2,500-ton hydraulic press (DCP-U 2500/2200, Dieffenbacher). PA66 pellets were dried using the dryer (LUXOR S 120, Motan Colotronic). The first extruder was a compounding twin screw extruder (ZSE-60HP-28D, Leistritz) with 60 mm diameter and length to diameter ratio (L/D) of 28; the second extruder was a mixing twin screw extruder (ZSG-75 P-17D, Leistritz) with 75 mm diameter and L/D of 17. The temperature of both extruders was 290 °C, and the screw speeds of the first and second extruders were 67.3 rpm and 36.1 rpm, respectively. Flow rate of material from the second extruder was 100.1 kg/h.

The length of the conveyer to the point where the plastificate was cut was approximately 50 cm, and conveyer belt temperature was set to 270 °C. For the hydraulic press, mold temperature was set to 120 °C, and force applied to the plastificate was set to 5,000 kN for 30 s.

Samples were collected from five locations along the D-LFT process line: (a) as received (i.e., virgin PA66), (b) directly after the first extruder (taken from the waterfall

film die), (c) directly after the second extruder, (d) when it was half-way along the conveyer (named half conveyer hereafter), and (e) a compressed plaque.

### 3.2.2 Triple detection gel permeation chromatography (GPC)

Absolute molecular weight distribution and intrinsic viscosity of the polymer matrix (i.e., PA66) were measured by gel permeation chromatography (GPC) coupled with triple detectors: a refractive index (RI) detector, a light scattering detector, and a four-capillary differential viscometer (Viscotek TDA302 and GPCmax, Malvern Panalytical). Potassium trifluoroacetate (KTFA) at 0.05 M concentration in 1,1,1,3,3,3-hexafluoro-2-propanol (HFIP) was employed as the mobile phase, and the flow rate was 0.7 mL/min. Samples were dissolved in HFIP and then filtered through a 0.22  $\mu\text{m}$  polytetrafluoroethylene (PTFE) syringe filter to remove any undissolved material. A 50  $\mu\text{L}$  sample was eluted through two columns held at 35°C. Poly(methyl methacrylate) (PMMA) standards were used for calibration.

The polydispersity index (*PDI*) of the polymer matrix (i.e., PA66) was calculated by

$$PDI = \frac{M_w}{M_n} \quad (10)$$

where  $M_w$  and  $M_n$  are, respectively, the weight-average molecular weight and the number-average molecular weight.

The intrinsic viscosity can be correlated with molecular weight using the following Mark-Houwink equation [22], [23]:

$$[\eta] = KM^\alpha \quad (11)$$

where  $K$  and  $\alpha$  are constants, and  $M$  is molecular weight.

The  $\alpha$  value is a function of polymer architecture, solvent used, and temperature [22], [23]. When branching occurs in the polymer, the  $\alpha$  value decreases provided that the same solvent is used and the temperature is fixed [23]. Therefore, the  $\alpha$  value was measured to examine if branching occurs through the D-LFT process. Eq. 2 can be transformed into the logarithmic form,

$$\log[\eta] = \log K + \alpha \log M \quad (12)$$

So that the  $\alpha$  value (slope) could be determined by plotting  $\log[\eta]$  against  $\log M$ .

### 3.2.3 Thermogravimetric analysis

The thermal stability of both polymer and composite samples was investigated using a thermogravimetric analyzer (TGA) (TGA Q50, TA Instruments). The mass of the samples was 8.5 mg ( $\pm 0.5$  mg). The temperature profile of the TGA analysis conducted was heating ramp of 10 °C/min from room temperature to 500 °C. The purge gas was nitrogen and flow rates were set to 40 mL/min and 60 mL/min to the balance and sample areas, respectively.

The degree of conversion (or decomposition),  $\alpha$ , of the sample was calculated by using:

$$\alpha = \left( \frac{M_o - M_t}{M_o - M_f} \right) \times 100 \quad (4)$$

where  $M_o$ ,  $M_t$ ,  $M_f$  are, respectively, the mass at the beginning of the decomposition profile, the corresponding mass at the decomposition level being calculated (e.g. mass when 20% decomposed), and the final mass after decomposition.

The activation energy for decomposition  $E_a$  was calculated from the TGA curves by the Horowitz-Metzger method [24]:

$$\ln[\ln(1 - \alpha)^{-1}] = \frac{E_a \theta}{R(T_{max})^2} \quad (5)$$

where  $\alpha$  is the degree of conversion (or decomposition),  $\theta$  is  $(T - T_{max})$  [K],  $T$  is the temperature [K],  $T_{max}$  is the temperature where the maximum rate of mass loss occurs [K], and  $R$  is the gas constant [8.31 J/(mol K)]. The activation energy for decomposition (slope) was determined by plotting  $\ln[\ln(1 - \alpha)^{-1}]$  versus  $\theta$ .

### 3.2.4 Differential scanning calorimetry

Non-isothermal and isothermal crystallization behaviors of the materials were studied using a differential scanning calorimeter (DSC) (Q2000, TA Instruments). A nitrogen purge gas with a flow rate of 50 mL/min was used. The mass of the samples was 8.5 mg ( $\pm 0.5$  mg) in both non-isothermal and isothermal measurements. In the non-isothermal crystallization measurements, a sample was first heated to 300 °C at 10 °C/min and held at that temperature for 5 minutes to erase the thermal history in the collected sample. The

sample was then cooled to 20 °C at 10 °C/min and held at that temperature for 5 minutes. Lastly, the sample was reheated to 300 °C at 10 °C/min. The degree of crystallinity  $X_c$  of the sample was calculated from the second DSC heating curve and the following equation:

$$X_c = \frac{\Delta H_m}{\Delta H_f(1 - W_f)} \times 100\% \quad (6)$$

where  $\Delta H_m$  is enthalpy of fusion;  $\Delta H_f$  is enthalpy of fusion of fully crystalline PA66, which is taken to be 191 J/g [10]; and  $W_f$  is the weight fraction of fiber.

In the isothermal crystallization measurements, a sample was first heated to 300 °C at 10 °C/min and held at that temperature for 5 minutes to erase the thermal history of the collected sample. Then, the sample was cooled to the isothermal temperature of 245 °C at 50 °C/min and held at that temperature for 30 minutes to allow the sample to fully crystallize. Using the isothermal DSC curves, relative degree of crystallinity  $X_{rel}$  was calculated as follows:

$$X_{rel} = \frac{\int_0^t \frac{dH(t)}{dt} dt}{\int_0^\infty \frac{dH(t)}{dt} dt} \quad (7)$$

where the isothermal DSC curve is integrated between  $t = 0$  and  $t$ , and divided by the overall crystallization area.

The crystallization kinetics were analyzed using the Avrami equation. According to the Avrami model [25], [26], the relative degree of crystallinity  $X_{rel}$  is described as follows:

$$X_{rel}(t) = 1 - \exp(-kt^n) \quad (8)$$

where  $n$  is the Avrami exponent that depends on the nucleation mechanism and growth geometry of crystals,  $k$  is the crystallization rate constant that involves both nucleation and growth rate parameters, and  $t$  is time.

Eq. 8 can be transformed into the double-logarithmic form,

$$\log[-\ln(1 - X_{rel}(t))] = \log k + n \log t \quad (9)$$

The parameters  $n$  (slope) and  $k$  (intercept) were determined by plotting  $\log[-\ln(1 - X_{rel}(t))]$  against  $\log t$ . The crystallization half time  $t_{1/2}$ , which is defined as the time from crystallization onset until 50% completion, was calculated as follows:

$$t_{1/2} = \left(\frac{\ln 2}{k}\right)^{\frac{1}{n}} \quad (10)$$

### 3.2.5 Fourier-transform infrared spectroscopy

Change in chemical structures of the polymer matrix (i.e., PA66) was studied by fourier transform infrared spectroscopy (FTIR) (Bruker Tensor II FTIR) equipped with a Hyperion 2000 microscope. Samples were dissolved in HFIP, and for samples with carbon fibers (i.e., samples after the second extruder), settled carbon fibers were removed from the solutions. A droplet of the PA66/HFIP solution was put on a potassium bromide window in the microscope and dried. Absorbance of the dried PA66 film sample was measured under a transmitted light mode in the wavenumber range of  $4000 \text{ cm}^{-1}$  to  $600 \text{ cm}^{-1}$ . The

resolution of wavenumber was  $4\text{ cm}^{-1}$  and thirty-two scans were averaged. The background spectra were corrected for the presence of  $\text{CO}_2$  and water vapour and baseline was corrected. Two areas on each film were analysed and the spectra were averaged.

### 3.3 Results and Discussion

#### 3.3.1 Discoloration

Samples collected up to the first extruder were pure PA66 and colorless, whereas those after the second extruder contained carbon fibers and these samples were black. In order to observe color changes of the PA66 matrix throughout the D-LFT process, samples collected from all the process locations were dissolved in HFIP, and for samples with carbon fibers (i.e., samples after the second extruder), settled carbon fibers were removed from the solutions. Figure 3.2 shows photographs of PA66/HFIP solutions for samples taken from different process locations along the D-LFT process. The solutions with the virgin PA66, first extruder, and second extruder samples were colorless and transparent. However, significant discolorations were observed in the solutions with the half conveyer and compressed plaque samples, and the compressed plaque samples were the darkest within the D-LFT process. The discolorations with the dark colors may have been caused by formation of char.

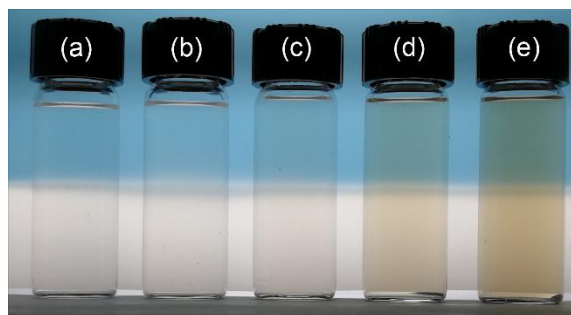


Figure 3.2 Material discoloration throughout the D-LFT process: (a) virgin PA66, (b) first extruder, (c) second extruder, (d) half conveyer, and (e) compressed plaque samples.

### 3.3.2 Molecular weight and intrinsic viscosity

Figure 3.3 shows weight-average molecular weight (Fig. 3.3a) and *PDI* (Fig. 3.3b) of the PA66 matrix in samples taken from different process locations along the D-LFT process. The molecular weight increased slightly with process progression up to the second extruder samples, increased significantly from the second extruder samples to the half conveyer samples, and increased further from the half conveyer samples to compressed plaque samples. As a consequence, molecular weight of the PA66 matrix increased drastically (by 122%) through the D-LFT process (i.e., from the virgin PA66 samples to the compressed plaque samples). A similar trend was observed for *PDI*, namely a continuous increase to the second extruder samples, a significant increase from the second extruder samples to the half conveyer samples, and a further increase from the half conveyer samples to compressed plaque samples.



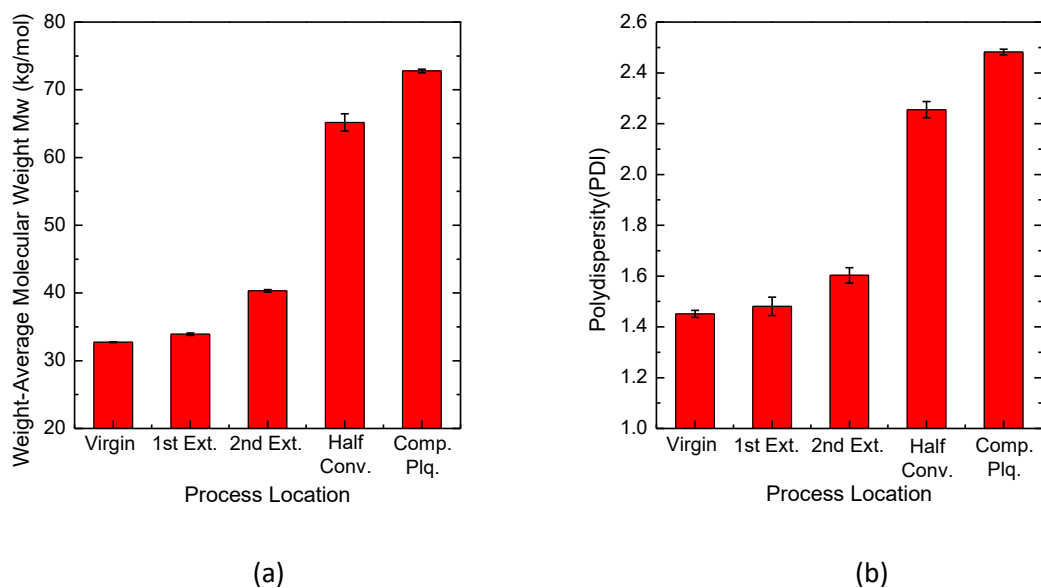


Figure 3.3 (a) Weight-average molecular weight and (b) PDI of the PA66 matrix in samples collected within the D-LFT process.

Figure 3.4a shows Mark-Houwink plots, that is, plots of  $\log[\eta]$  versus  $\log M$ , of the PA66 matrix in samples taken from different process locations. There were two distinct groups of lines. One group includes samples in the earlier stages of the D-LFT process (i.e., the virgin, first extruder, and second extruder samples), and the other group has samples from the later stage of the D-LFT process (i.e., the half conveyer and compressed plaque samples). Figure 3.4b shows the slopes from the Mark-Houwink plots (i.e.,  $\alpha$  values). The  $\alpha$  value decreased slightly with process progression up to the second extruder samples, decreased significantly from the second extruder samples to the half conveyer samples, and remained nearly unchanged from the half conveyer samples to the compressed plaque samples. The results suggest that branching of PA66 molecules occurred through the D-LFT process, especially from the second extruder samples to the half conveyer samples.

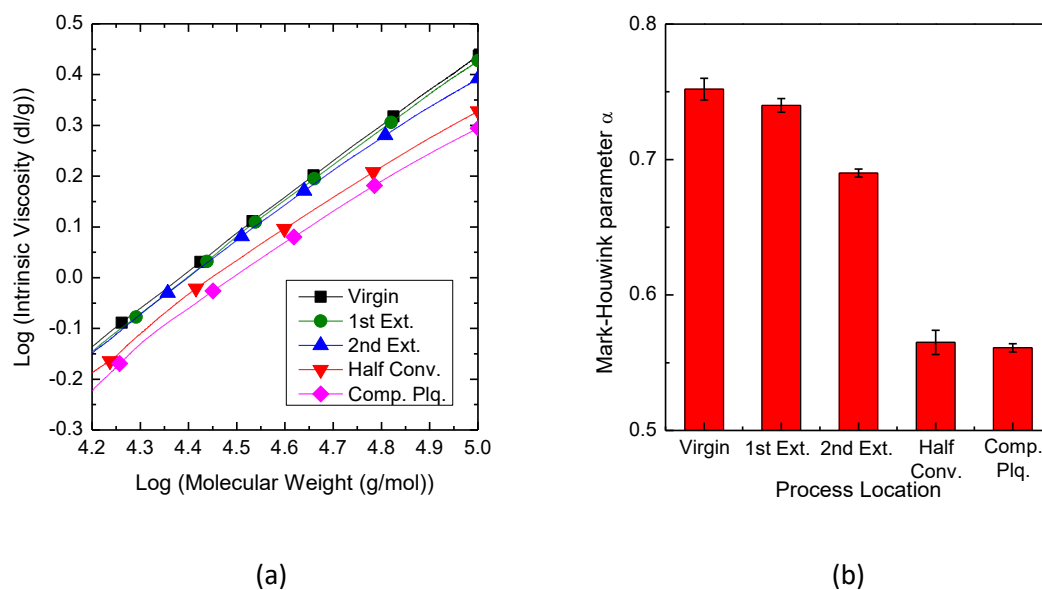


Figure 3.4 (a) Mark-Houwink plots and (b)  $\alpha$  values obtained from Mark-Houwink plots of the PA66 matrix in samples collected within the D-LFT process.

### 3.3.3 Fourier-transform infrared spectroscopy

Figure 3.5a shows FTIR spectra of the PA66 matrix in samples taken from different process locations along the D-LFT process. The figure indicates major characteristic bands of PA66: the amide N-H stretching at  $3303\text{ cm}^{-1}$ ,  $\text{CH}_2$  asymmetric stretching at  $2934\text{ cm}^{-1}$ , and  $\text{CH}_2$  symmetric stretching at  $2860\text{ cm}^{-1}$ , the amide I at  $1639\text{ cm}^{-1}$ , and amide II at  $1543\text{ cm}^{-1}$  [27]. Figure 3.5b shows how the amide N-H stretching peaks changed through the D-LFT process. Intensity of the peak values remained unchanged from the virgin samples to the first extruder samples and increased slightly from the first extruder samples to the second extruder samples, whereas intensity of the peak values decreased continuously from the second extruder samples to the compressed plaque samples. It is noted that molten composites were exposed to atmosphere after ejection from the second extruder; therefore, hydrolysis of the PA66 matrix may have been encouraged with water vapor in the

atmosphere, which is supported by the decrease of the amide N-H stretching peak intensity from the second extruder samples to the compressed plaque samples.

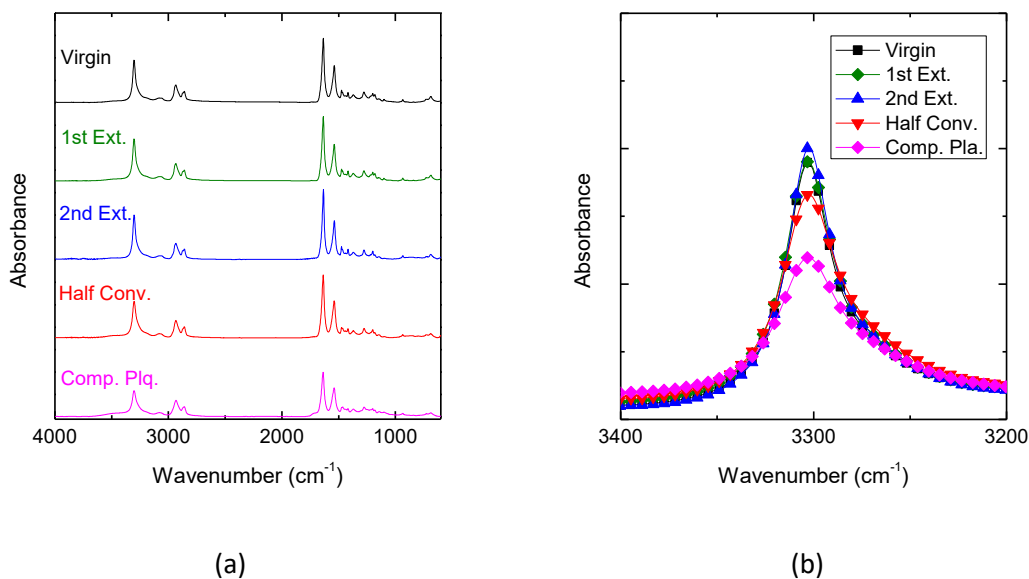


Figure 3.5 (a) FTIR spectra and (b) amide N-H stretching peaks of the PA66 matrix in samples collected within the D-LFT process.

### 3.3.4 Mechanism of increase in molecular weight of PA66 matrix

A unique process condition of the D-LFT process is that the molten composite are exposed to atmosphere such as water vapor and oxygen, especially after the second extruder, where the significant increase of molecular weight (Fig. 3.3a) and branching (Fig. 3.4b) of the PA66 matrix were observed. These increases could be explained by a series of chemical reactions: hydrolysis, thermal-oxidation, and grafting, as shown in Figure 3.6. When the PA66 matrix was exposed to water vapor in the atmosphere, amine end-groups and carboxylic acid end-groups of PA66 molecules were produced through hydrolytic scission of amide bond C(O)-NH [9], [28], [29]. On the other hand, when the PA66 matrix was

exposed to oxygen in the atmosphere, methylene groups (preferentially  $\beta$ -positioned) in PA66 molecules could be oxidized and ketonic carbonyl groups could be formed [9], [28], [30]. The ketonic carbonyl groups of PA66 molecules could provide sites for grafting of the PA66 molecules. The amine end-groups of the hydrolyzed PA66 molecules could react with the ketonic carbonyl groups in the oxidized PA66 to form branch structure of PA66 molecules [9], [28], [30], thus increasing molecular weight of the PA66 molecules.

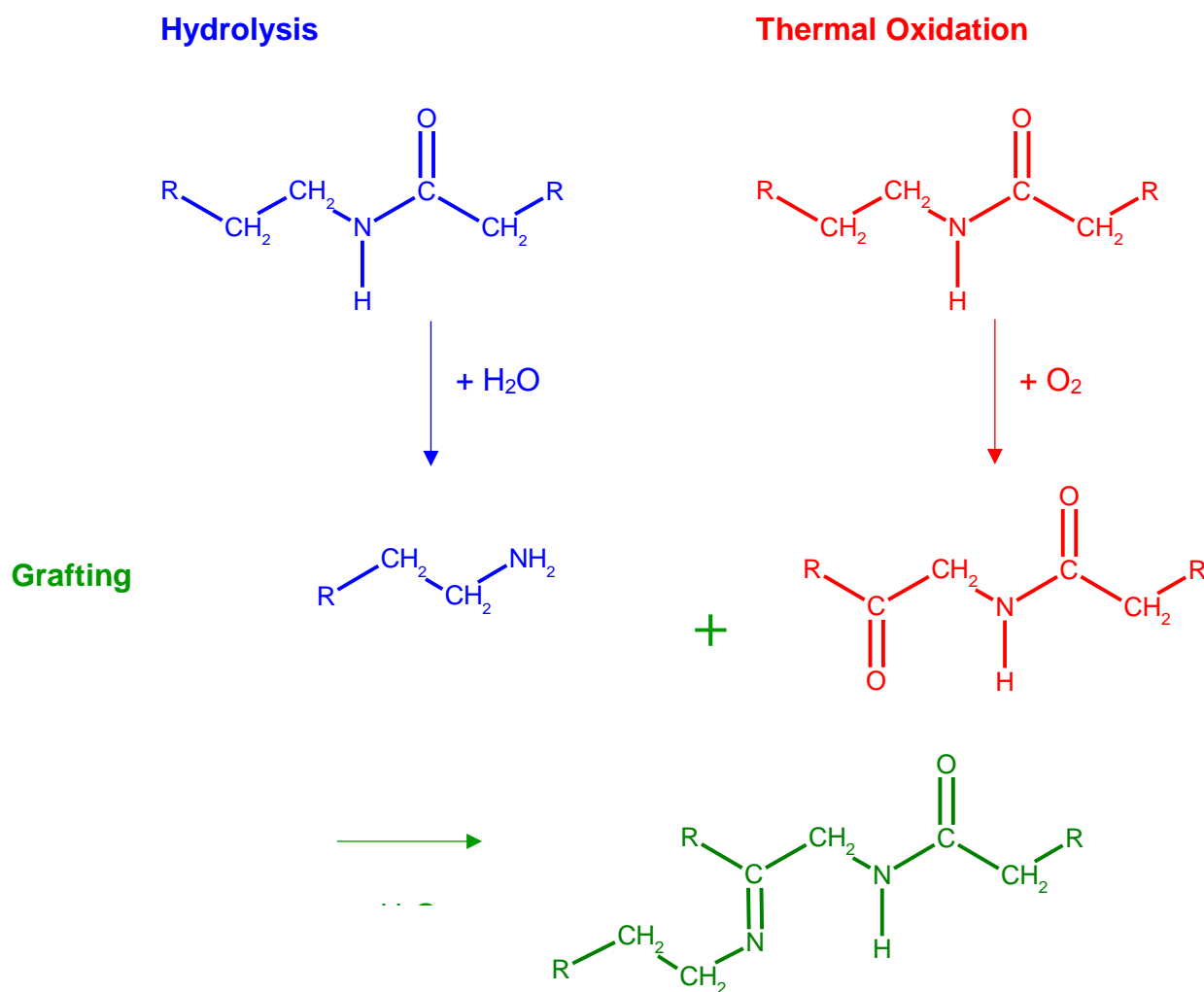


Figure 3.6 Mechanism of increase in molecular weight of the PA66 matrix.

### 3.3.5 Thermal decomposition

Figure 3.7 shows typical thermogravimetric profiles obtained from samples collected from different process locations along the D-LFT process. The figure indicates that all the samples had a single-stage decomposition of the PA66 matrix. Figure 3.8a shows typical Horowitz-Metzger plots, that is, plots of  $\ln[\ln(1 - \alpha)^{-1}]$  versus  $\theta$ . The figure indicates that the trend lines for all the samples were almost linear, and the slope decreased with process progression up to the half conveyer samples. The slopes of trend lines were used to calculate activation energy.

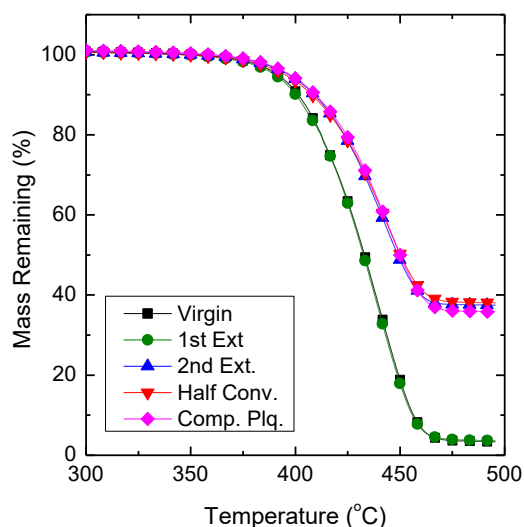


Figure 3.7 TGA curves of materials collected within the D-LFT process.

Figure 3.8b shows the activation energy of samples collected from different process locations. The activation energy decreased with process progression from the virgin samples to the half conveyer samples, which may be attributed to the change in molecular structure of the PA66 matrix. Branching of the PA66 matrix occurred from the virgin samples to the half conveyer samples (see Fig. 3.4b). Such molecules may be less thermally

stable (i.e., lower activation energy) than the original, liner structure of the PA66 matrix. However, the activation energy increased with further process progression from the half conveyer samples to the compressed plaque samples. It should be noted that, as shown in Figure 3.2, significant discoloration occurred in the compressed plaque samples. It is known that the formation of char can increase the activation energy [20], [31]. Therefore, it is surmised that the positive effect of the char formation may have surpassed the negative effect of the molecular changes of the PA66 matrix, thus leading to the increase of activation energy from the half conveyer samples to the compressed plaque samples.

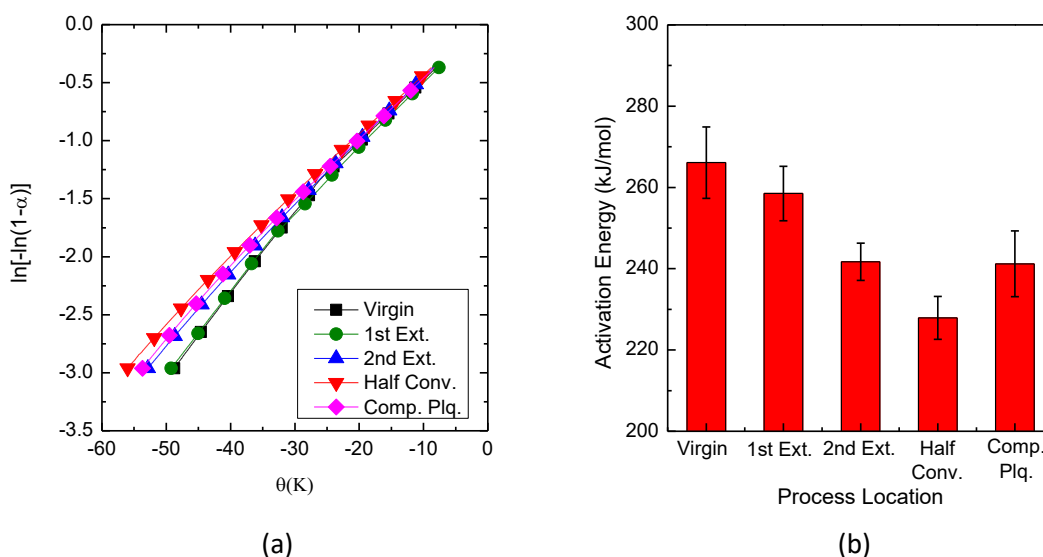


Figure 3.8 (a) Horowitz-Metzger plots of materials collected within the D-LFT process and (b) activation energy of materials collected within the D-LFT process.

### 3.3.6 Crystallization

#### 3.3.6.1 Non-Isothermal Crystallization

Figure 3.9 shows typical non-isothermal DSC cooling curves (Fig. 3.9a) and subsequent heating curves (Fig. 3.9b) of samples collected from different process locations along the D-LFT process. Table 3.1 summarizes the thermal properties that were obtained from the

DSC cooling and heating curves, including the crystallization peak temperature ( $T_c$ ), the enthalpy of crystallization ( $\Delta H_c$ ), the melting peak temperatures ( $T_{m1}$ ,  $T_{m2}$ ), the enthalpy of fusion ( $\Delta H_m$ ) and the degree of crystallinity ( $X_c$ ). The table suggests that the crystallization peak temperature, obtained from the DSC cooling curves, remained constant throughout the D-LFT process.

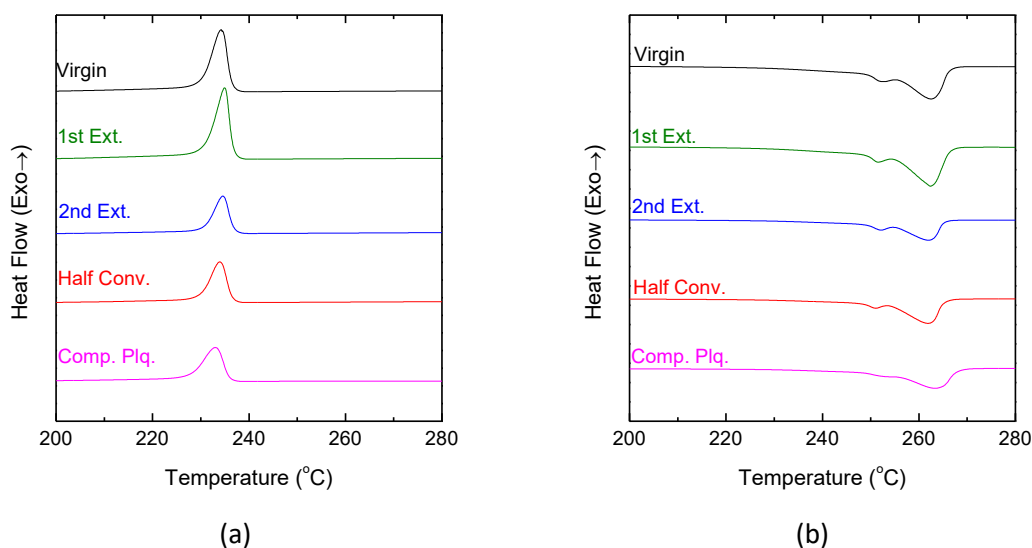


Figure 3.9 Non-isothermal DSC curves of materials collected within the D-LFT process: (a) cooling curves and (b) heating curves.

Table 3.1 Non-isothermal crystallization data of materials collected within the D-LFT process. The numbers in the parenthesis are the standard deviations ( $n \geq 3$ ).

Process Location	$T_c$ (°C)	$\Delta H_c$ (J/g)	$T_{m1}$ (°C)	$T_{m2}$ (°C)	$\Delta H_m$ (J/g)	$X_c$ (%)
Virgin	234.8 (0.5)	56.4 (2.1)	252.1 (0.4)	262.5 (0.3)	79.6 (2.0)	41.7% (1.0%)
1st Extruder	234.5 (0.5)	63.5 (6.4)	251.5 (0.3)	262.3 (0.2)	79.1 (5.1)	41.4% (2.7%)
2nd Extruder	234.5 (0.2)	31.8 (3.3)	251.8 (0.3)	261.8 (0.3)	46.5 (5.9)	38.2% (4.9%)
Half Conveyer	234.2 (0.4)	34.3 (2.7)	251.1 (0.1)	261.8 (0.4)	47.6 (4.0)	40.1% (3.4%)
End Compressed Plaque	233.6 (0.4)	33.7 (3.1)	251.3 (1.2)	261.9 (0.9)	47.7 (4.6)	40.35% (3.9%)

Two melting peaks ( $T_{m1}$  and  $T_{m2}$ , where  $T_{m1} < T_{m2}$ ) were observed on the DSC heating curves.  $T_{m1}$  and  $T_{m2}$  are associated with melting temperatures of the  $\beta$  form and  $\alpha$  form of PA66 crystallites, respectively. In the  $\alpha$  form successive layers (i.e., sheets of molecules) are displaced always in the same direction by a fixed distance while in the  $\beta$  form successive layers are displaced alternately up and down by the same distance [32]. The data suggests that the two melting peaks stayed unchanged throughout the process. In addition, the calculated degree of crystallinity  $X_c$  for each of the process locations is shown in Table 3.1. Degree of crystallinity values were similar among the different process locations.

### 3.3.6.2 Isothermal Crystallization

Figure 3.10 shows typical isothermal DSC curves of samples collected from different process locations along the D-LFT process. The figure suggests that crystallization speed of samples decreased as a whole through the D-LFT process, though the speed increased slightly from the first extruder samples to the second extruder and remained same from the half conveyer samples to the compressed plaque samples. Figure 3.11a shows typical Avrami plots, that is, plots of  $\log[-\ln(1 - X_{rel}(t))]$  versus  $\log t$ . The kinetic parameters determined using Avrami plots are summarized in Table 3.2. The Avrami exponent,  $n$ , changed little along the DLT process, which suggests that crystal nucleation mechanism of PA66 changed little along the DLT process and the addition of carbon fibers had little influence on the crystal nucleation mechanism of PA66.



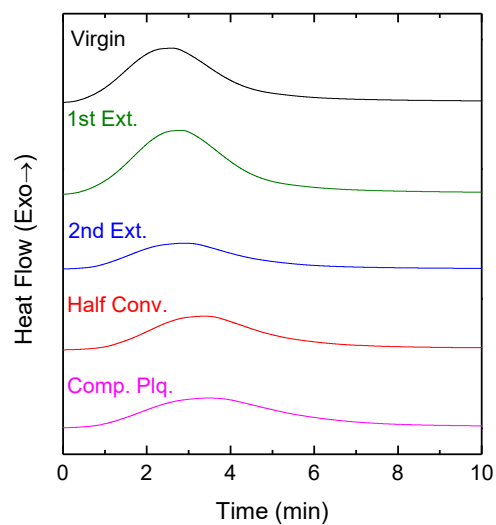


Figure 3.10 Isothermal DSC curves of materials collected within the D-LFT process.

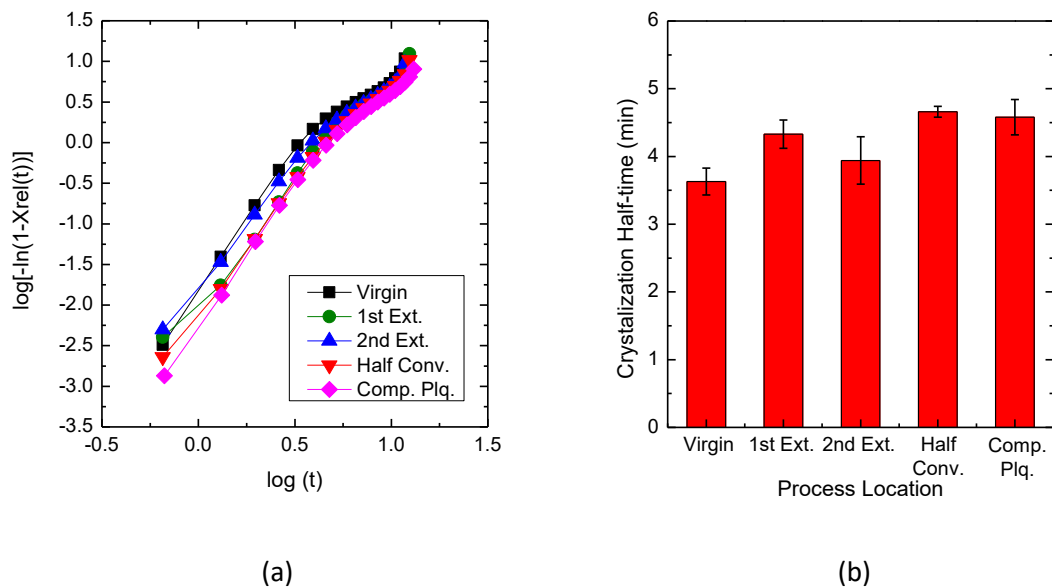


Figure 3.11 (a) Avrami plots of materials collected within the D-LFT process and (b) crystallization half-time of materials collected within the D-LFT process.

Table 3.2 Avrami parameters of materials collected within the D-LFT process. The numbers in the parenthesis are the standard deviations ( $n \geq 3$ ).

<b>Process Location</b>	<b><i>n</i></b>	<b><i>k</i> (min<sup>-n</sup>)</b>
<b>Virgin</b>	2.53 (0.14)	$2.75 \times 10^{-2}$ ( $8.2 \times 10^{-3}$ )
<b>First Extruder</b>	2.96 (0.17)	$1.39 \times 10^{-2}$ ( $4.0 \times 10^{-3}$ )
<b>Second Extruder</b>	2.49 (0.12)	$2.37 \times 10^{-2}$ ( $7.1 \times 10^{-3}$ )
<b>Half Conveyer</b>	2.68 (0.13)	$1.13 \times 10^{-2}$ ( $2.2 \times 10^{-3}$ )
<b>Compressed Plaque</b>	2.71 (0.17)	$1.19 \times 10^{-2}$ ( $4.1 \times 10^{-3}$ )

Figure 3.11b shows the crystallization half-time from samples collected from different process locations. The crystallization half-time increased from the virgin samples to the first extruder samples. The increase of crystallization half-time in the first extruder samples may have been caused by branching of PA66 (see Fig. 3.4b). With process progression, the crystallization half-time decreased from the first extruder samples to the second extruder samples. There may be two main factors to have affected crystallization half-time in the second extruder samples: (1) branching of PA66 and (2) heterogeneous nucleation caused by carbon fibers. It is noted that the carbon fibers were introduced to the PA66 in the second extruder. It was reported that fibers, when introduced to a polymer, acted as heterogeneous nucleating agents (NA) during crystallization [33]. If the fibers did act in such a way, they may have provided nucleation sites for crystal growth and decreased the crystallization half-time. It is speculated that the heterogeneous nucleation caused by carbon fibers had a greater influence on the crystallization half-time than branching of PA66, thus decreasing crystallization half-time in the second extruder samples. With further process progression, the crystallization half-time increased from the second

extruder samples to the half conveyer samples, where extensive branching of the PA66 matrix occurred. The chain branching interferes with chain folding of the PA66 matrix, thus increasing the crystallization half-time. In the final process stage, the crystallization half-time was little changed from the half conveyer to the compression molding, where the degree of branching of PA66 remained nearly unchanged (see Fig. 3.4b).

### 3.4 Conclusions

Effects of the D-LFT process on the molecular weight of the PA66 matrix and thermal properties of carbon fiber reinforced PA66 were studied at the five locations. Triple Detection GPC results showed that molecular weight of the PA66 matrix increased drastically (by 122%) due to branching of the molecules through the D-LFT process. Molecular weight increased slightly with process progression up to the second extruder samples and a significant increase was observed from the second extruder samples to the compressed plaque samples. TGA results showed that activation energy for decomposition decreased continuously up to the half conveyer samples, but increased from the half conveyer samples to the compressed plaque samples possibly owing to char formation. Non-isothermal DSC crystallization analysis revealed no substantial changes to the degree of crystallinity throughout the D-LFT process. However, isothermal DSC crystallization analysis showed that crystallization half-time was increased by branching of PA66 molecules through the D-LFT process, though carbon fibers may have acted as heterogeneous nucleating agents.

## References

- [1] W. Krause, F. Henning, S. Tröster, O. Geiger, and P. Eyerer, “LFT-D — A Process Technology for Large Scale Production of Fiber Reinforced Thermoplastic Components,” *J. Thermoplast. Compos. Mater.*, vol. 16, no. 4, pp. 289–302, Jul. 2003.
- [2] M. Schemme, “LFT – development status and perspectives,” *Reinf. Plast.*, vol. 52, no. 1, pp. 32–39, Jan. 2008.
- [3] H. Ning, N. Lu, A. A. Hassen, K. Chawla, M. Selim, and S. Pillay, “A review of Long fibre thermoplastic (LFT) composites,” *Int. Mater. Rev.*, vol. 64, pp. 1–25, Mar. 2019.
- [4] T. Whitfield, T. Kuboki, J. Wood, V. Ugresic, S. Sathyanarayana, and K. Dagnon, “Thermal properties of glass fiber reinforced polyamide 6 composites throughout the direct long-fiber reinforced thermoplastic process,” *Polym. Eng. Sci.*, vol. 58, no. 1, pp. 46–54, Jan. 2018.
- [5] T. Whitfield, T. Kuboki, J. Wood, V. Ugresic, S. Sathyanarayana, and K. Dagnon, “Effects of process parameters on thermal properties of glass fiber reinforced polyamide 6 composites throughout the direct long-fiber-reinforced thermoplastics process,” *Polym. Eng. Sci.*, vol. 58, no. S1, pp. E114–E123, May 2018.
- [6] S. Chand, “Review Carbon fibers for composites,” *J. Mater. Sci.*, vol. 35, no. 6, pp. 1303–1313, 2000.
- [7] S. Park, *Carbon Fibers*. Dordrecht, Netherlands: Springer, 2015.

- [8] S. M. Aharoni, *n-Nylons: their synthesis, structure and properties*. Chichester, England: John Wiley & Sons Ltd, 1997.
- [9] S. V Levchik, E. D. Weil, and M. Lewin, "Thermal decomposition of aliphatic nylons," *Polym. Int.*, vol. 48, no. 7, pp. 532–557, 1999.
- [10] J. Brandrup, E. H. Immergut, and E. A. Grulke, Eds., *Polymer handbook*, 4th ed. New York, USA: John Wiley & Sons, Inc., 1999.
- [11] F. Chavarria and D. R. Paul, "Comparison of nanocomposites based on nylon 6 and nylon 66," *Polymer (Guildf.)*, vol. 45, no. 25, pp. 8501–8515, 2004.
- [12] M. I. Kohan, *Nylon Plastics Handbook*. New York, USA: Hanser Publishers, 1995.
- [13] B. J. Holland and J. N. Hay, "Thermal degradation of nylon polymers," *Polym. Int.*, vol. 49, no. 9, pp. 943–948, 2000.
- [14] R. S. Lehrle, I. W. Parsons, and M. Rollinson, "Thermal degradation mechanisms of Nylon 6 deduced from kinetic studies by pyrolysis-g.c.," *Polym. Degrad. Stab.*, vol. 67, no. 1, pp. 21–33, 2000.
- [15] A. G. Pedroso, L. H. I. Mei, J. A. M. Agnelli, and D. S. Rosa, "The influence of the drying process time on the final properties of recycled glass fiber reinforced polyamide 6," *Polym. Test.*, vol. 21, no. 2, pp. 229–232, 2002.
- [16] R. D. Davis, J. W. Gilman, and D. L. VanderHart, "Processing degradation of polyamide 6/montmorillonite clay nanocomposites and clay organic modifier," *Polym. Degrad. Stab.*, vol. 79, no. 1, pp. 111–121, 2003.

- [17] K. Pielichowski and J. Njuguna, *Thermal Degradation of Polymeric Materials*. Shawbury, UK: Rapra Technology Limited, 2005.
- [18] C. L. Beyler and M. M. Hirschler, "Thermal Decomposition of Polymers," in *SFPE Handbook of Fire Protection Engineering*, 4th ed., Quincy, USA: National Fire Protection Association, 2008, pp. 110–131.
- [19] J. E. Crespo, F. Parres, M. A. Peydró, and R. Navarro, "Study of rheological, thermal, and mechanical behavior of reprocessed polyamide 6," *Polym. Eng. Sci.*, vol. 53, no. 4, pp. 679–688, Apr. 2013.
- [20] X. Zuo, H. Shao, D. Zhang, Z. Hao, and J. Guo, "Effects of thermal-oxidative aging on the flammability and thermal-oxidative degradation kinetics of tris(tribromophenyl) cyanurate flame retardant PA6/LGF composites," *Polym. Degrad. Stab.*, vol. 98, no. 12, pp. 2774–2783, 2013.
- [21] L. Xia, B. Shentu, and Z. Weng, "Preparation of a novel stabilizer and its thermal-oxidative stabilization effect on polyamide 6," *Polym. Eng. Sci.*, vol. 54, no. 9, pp. 2197–2206, Sep. 2014.
- [22] P. C. Hiemenz and T. Lodge, *Polymer chemistry*, 2nd ed. Boca Raton, FL, USA: Taylor & Francis, 2007.
- [23] A. M. Striegel, W. W. Yau, J. J. Kirkland, and D. D. Bly, *Modern Size-Exclusion Liquid Chromatography*, 2nd ed. Hoboken, NJ, USA: John Wiley & Sons, Inc., 2009.

- [24] H. H. Horowitz and G. Metzger, "A New Analysis of Thermogravimetric Traces," *Anal. Chem.*, vol. 35, no. 10, pp. 1464–1468, 1963.
- [25] M. Avrami, "Kinetics of Phase Change. II Transformation-Time Relations for Random Distribution of Nuclei," *J. Chem. Phys.*, vol. 8, no. 212, pp. 212–224, 1940.
- [26] M. Avrami, "Granulation, Phase Change, and Microstructure Kinetics of Phase Change. III," *J. Chem. Phys.*, vol. 9, no. 2, pp. 177–184, 1941.
- [27] S. J. Cooper, M. Coogan, N. Everall, and I. Priestnall, "A polarised  $\mu$ -FTIR study on a model system for nylon 6 6: implications for the nylon Brill structure," *Polymer (Guildf.)*, vol. 42, no. 26, pp. 10119–10132, 2001.
- [28] A. L. Bhuiyan, "Some aspects of the thermal stability action of the structure in aliphatic polyamides and polyacrylamides," *Polymer (Guildf.)*, vol. 25, no. 12, pp. 1699–1710, 1984.
- [29] P. R. Hornsby, J. Wang, R. Rother, G. Jackson, G. Wilkinson, and K. Cossick, "Thermal decomposition behaviour of polyamide fire-retardant compositions containing magnesium hydroxide filler," *Polym. Degrad. Stab.*, vol. 51, no. 3, pp. 235–249, 1996.
- [30] T. Karstens and V. Rossbach, "Thermo - oxidative degradation of polyamide 6 and 6,6. Kinetics of the formation and inhibition of UV/VIS - active chromophores," *Die Makromol. Chemie*, vol. 190, no. 12, pp. 3033 – 3053, Jun.

1989.

- [31] K. Scully and R. Bissessur, "Decomposition kinetics of nylon-6/graphite and nylon-6/graphite oxide composites," *Thermochim. Acta*, vol. 490, no. 1–2, pp. 32–36, 2009.
- [32] C. W. Bunn and E. V Garner, "The crystal structures of two polyamides ('nylons')," *Proc. R. Soc. London. Ser. A. Math. Phys. Sci.*, vol. 189, no. 1016, pp. 39–68, 2006.
- [33] N. Klein, D. Selivansky, and G. Marom, "The effects of a nucleating agent and of fibers on the crystallization of nylon 66 matrices," *Polym. Compos.*, vol. 16, no. 3, pp. 189–197, Jun. 1995.



## Chapter 4

### 4 Conclusions and Recommendations for Future Study

#### 4.1 Conclusions

The D-LFT process is an efficient and cost-effective process and includes two twin-screw extruders, a conveyor, and a compression molding machine. Polyamides (PAs) are good candidates as a polymer matrix for D-LFT products because they have good mechanical properties, thermal properties, wear resistance, chemical resistance, and fire resistance. However, PAs are susceptible to heat. Therefore, it is important to study how the process sequence affects molecular weight and thermal properties of PA-based composite materials during the D-LFT process. The main objective of this study was to characterize variation in molecular weight and thermal properties of two types of PA-based composite materials (glass fiber reinforced PA6 composites and carbon fiber reinforced PA66 composites) through the D-LFT process.

First, variation in molecular weight and thermal properties of glass fiber reinforced PA6 composites were investigated throughout the D-LFT process. Two screw configurations, which generate low and high shear stress in composite melt (named the conveying and mixing screws, respectively), were used in the second twin-screw extruder, where continuous fibers were mixed with polymer melt. Samples were taken from four different locations along the D-LFT process and characterized using triple detection GPC, TGA, and DSC. The results suggested that the molecular weight of the PA6 matrix increased in the later stages of the D-LFT process (i.e., after the second extruder) by branching of PA6 molecules. Activation energy for decomposition decreased continuously

up to the second extruder, but nearly unchanged (or only slightly increased) from the second extruder to the compression molding. The degree of crystallinity remained unchanged; however, the crystallization half-time was decreased up to the second extruder and unchanged from the second extruder to the compression molding. In addition, the mixing screw decreased the molecular weight of the PA6 matrix more than the conveying screw. However, such a decrease in molecular weight had little influence on the thermal stability and crystallization behavior of the composites.

Second, variation in molecular weight and thermal properties of carbon fiber reinforced PA66 composites were studied throughout the D-LFT process. Samples were taken from five different locations along the D-LFT process and characterized using triple detection GPC, TGA, DSC, and FTIR. The results suggested that molecular weight of the PA66 matrix was increased drastically (by 122%) by branching of PA66 molecules through the D-LFT process and a significant increase was observed in the later stages of the D-LFT process (i.e., after the second extruder). Activation energy for decomposition decreased continuously up to the halfway point of the conveyer, but increased from the half conveyer to the compression molding. The degree of crystallinity remained unchanged; however, the crystallization half-time was increased by branching of PA66 molecules through the D-LFT process.

In conclusion, it was found that molecular weight of both glass fiber reinforced PA6 composites and carbon fiber reinforced PA66 composites increased after the second extruder by branching of PA molecules. In particular, carbon fiber reinforced PA66 composites had significant increase of molecular weight and branching. Due to the difference in degree of branching, crystallization half-time of glass fiber reinforced PA6

composites decreased along the D-LFT process, whereas that of carbon fiber reinforced PA66 composites increased. It is expected that molecular weight and structure of PAs affect other physical properties of D-LFT products. Therefore, process conditions after the second extruder, such as temperature and residence time of the conveyer, need to be carefully adjusted to design PA-based D-LFT products.

## 4.2 Contributions

This is the first study to investigate (i) the effects of extruder screw configurations on thermal properties of glass fiber-reinforced PA6 composites and (ii) thermal properties of carbon fiber reinforced PA66 composites throughout the D-LFT process. Furthermore, very unique phenomenon was observed in the D-LFT process; molecular weight of the PA66 matrix increased significantly after the second extruder in the D-LFT process. The mechanism for the significant increase in molecular weight of the PA66 matrix was proposed with a series of chemical reactions occurred during the D-LFT process.

## 4.3 Recommendations for Future Study

The recommended future studies are described as follows:

- (1) This study suggested that branching of PAs occurred when the molten composite is exposed to atmosphere. Therefore, effects of temperature and time on molecular weight and branching of PAs need to be investigated under atmosphere. The study will provide useful information to design the D-LFT process of PA-based D-LFT products.

- (2) This study suggested that molecular weight of PAs was increased by branching of the molecules after the second extruder, where continuous fibers were mixed with polymer melt. These increases could be caused by a series of chemical reactions and fibers may have affected the chemical reactions. A carbon fiber has a faster electron transfer rate due to its graphitic structure, whereas a glass fiber does not transfer electrons. Therefore, effects of fiber on molecular weight and structure of PAs needs to be studied.
- (3) This study proposed branching mechanisms of PA66. In order to support the proposed mechanisms, FTIR was used to observe changes of chemical bonds. Nuclear magnetic resonance spectroscopy (NMR) is another technique which may provide additional information of chemical structures of PA66. In addition, the proposed series of chemical reactions may be verified using tracing techniques such as isotopic labeling. By replacing atoms with their isotopes, routes of the atoms transferred in the reaction can be traced using FTIR, NMR, and mass spectrometry (MS).
- (4) In this study, it was postulated that formation of char may have caused the increased activation energy for decomposition. There may be a relationship between degree of branching of PAs and amount of char generated. Further study is need to investigate the relationship and mechanisms of char formation.

## Curriculum Vitae

**Name:** Mingyu Yang

**Post-secondary Education and Degrees:** The University of Western Ontario  
London, Ontario, Canada  
May 2012 - June 2016 B.E.Sc.  
Jan. 2017 – present M.E.Sc.

**Related Work Experience:** Teaching Assistant  
The University of Western Ontario  
2018-2019

### Publications:

Yang, M., Kuboki, T., Wood, J., Ugresic, V. Effects of Extruder Screw Configurations on Thermal Properties of Glass Fiber-Reinforced Polyamide 6 Composites throughout the Direct Long-Fiber-Reinforced Thermoplastics Process. *Polymer Composites*, Accepted, 2018. doi: 10.1002/pc.25212.

Yang, M., Kuboki, T., Wood, J., and Ugresic, V. Thermal Properties of Carbon Fiber Reinforced Polyamide 66 Composites throughout the Direct Long-Fiber-Reinforced Thermoplastics Process. Annual Technical Conference 2019 of Society of Plastics Engineers, 18-21 March 2019, Detroit, Michigan, USA.

(Poster) Yang, M., Kuboki, T., Wood, J., and Ugresic, V. Effects of Extruder Screw Configurations on Thermal Stability and Crystallization Behavior of Glass Fiber Reinforced Polyamide 6 Composites throughout the Direct Long-Fiber Reinforced Thermoplastics Process. Automotive Composites Conference and Exhibition 2018 of Society of Plastics Engineers, 5-7 September 2018, Novi, Michigan, USA.

Yang, M., Kuboki, T., Wood, J., Ugresic, V., Sathyanarayana, S., and Dagnon, K. Effects of Extruder Screw Configuration on Thermal Properties of Glass Fiber Reinforced Polyamide 6 Composites throughout the Direct Long-Fiber-Reinforced Thermoplastics Process. Annual Technical Conference 2018 of Society of Plastics Engineers, 7-10 May 2018, Orlando, Florida, USA.